A comparison of classification techniques for seismic facies recognition

Tao Zhao[1], Vikram Jayaram[2], Atish Roy[3], and Kurt J. Marfurt[1]

Abstract

During the past decade, the size of 3D seismic data volumes and the number of seismic attributes have increased to the extent that it is difficult, if not impossible, for interpreters to examine every seismic line and time slice. To address this problem, several seismic facies classification algorithms including k-means, self-organizing maps, generative topographic mapping, support vector machines, Gaussian mixture models, and artificial neural networks have been successfully used to extract features of geologic interest from multiple volumes. Although well documented in the literature, the terminology and complexity of these algorithms may bewilder the average seismic interpreter, and few papers have applied these competing methods to the same data volume. We have reviewed six commonly used algorithms and applied them to a single 3D seismic data volume acquired over the Canterbury Basin, offshore New Zealand, where one of the main objectives was to differentiate the architectural elements of a turbidite system. Not surprisingly, the most important parameter in this analysis was the choice of the correct input attributes, which in turn depended on careful pattern recognition by the interpreter. We found that supervised learning methods provided accurate estimates of the desired seismic facies, whereas unsupervised learning methods also highlighted features that might otherwise be overlooked.

Introduction

In 2015, pattern recognition has become part of everyday life. Amazon or Alibaba analyzes the clothes you buy, Google analyzes your driving routine, and your local grocery store knows the kind of cereal you eat in the morning. "Big data" and "deep learning algorithms" are being analyzed by big companies and big government, attempting to identify patterns in our spending habits and the people with whom we associate.

Successful seismic interpreters are experts at pattern recognition: identifying features such as channels, mass transport complexes, and collapse features, where our engineering colleagues only see wiggles. Our challenge as interpreters is that the data volumes we need to analyze keep growing in size and dimensionality, whereas the number of experienced interpreters has remained relatively constant. One solution to this dilemma is for these experienced interpreters to teach their skills to the next generation of geologists and geophysicists, either through traditional or on-the-job training. An alternative and complementary solution is for these experienced interpreters to teach theirs skills to a machine. Turing (1950), whose scientific contributions and life has recently been popularized in a movie, asks whether machines can think. Whether machines will ever be able to think is a question for scientists and philosophers to answer (e.g., Eagleman, 2012), but machines can be taught to perform repetitive tasks, and even to unravel the relationships that underlay repetitive patterns, in an area called *machine learning*.

Twenty-five years ago, skilled interpreters delineated seismic facies on a suite of 2D lines by visually examining seismic waveforms, frequency, amplitude, phase, and geometric configurations. Facies would then be posted on a map and hand contoured to generate a seismic facies map. With the introduction of 3D seismic data and volumetric attributes, such analysis has become more quantitative and more automated. In this tutorial, we focus on classification (also called *clustering*) on large 3D seismic data, whereby like patterns in the seismic response (seismic facies) are assigned similar values. Much of the same technology can be used to define specific rock properties, such as brittleness, total organic content, or porosity. Pattern recognition and clustering are common to many industries, from using cameras to identify knotholes in plywood production, to tracking cell phone communications, to identifying potential narcotics traffickers. The workflow is summarized in the classic textbook by Duda et al. (2001) displayed in Figure 1. In this figure, "sensing" consists of

[1]The University of Oklahoma, ConocoPhillips School of Geology and Geophysics, Norman, Oklahoma, USA. E-mail: tao-zhao@ou.edu; kmarfurt@ou.edu.

[2]Oklahoma Geological Survey, Norman, Oklahoma, USA. E-mail: vjayaram@ou.com.

[3]BP America, Houston, Texas, USA. E-mail: atish.roy@bp.com.

Manuscript received by the Editor 19 February 2015; revised manuscript received 2 May 2015; published online 14 August 2015. This paper appears in *Interpretation*, Vol. 3, No. 4 (November 2015); p. SAE29–SAE58, 30 FIGS., 3 TABLES.

http://dx.doi.org/10.1190/INT-2015-0044.1.

seismic, well log, completion, and production measurements. For interpreters, "segmentation" will usually mean focusing on a given stratigraphic formation or suite of formations. Seismic data lose their temporal and lateral resolution with depth, such that a given seismic facies changes its appearance, or is nonstationary, as we go deeper in the section. The number of potential facies also increases as we analyze larger vertical windows incorporating different depositional environments, making classification more difficult. For computer-assisted facies classification, "feature extraction" means attributes, be they simple measurements of amplitude and frequency; geometric attributes that measure reflector configurations; or more quantitative measurements of lithology, fractures, or geomechanical properties provided by prestack inversion and azimuthal anisotropy analysis. "Classification" assigns each voxel to one of a finite number of classes (also called *clusters*), each of which represents a seismic facies that may or may not correspond to a geologic facies. Finally, using validation data, the interpreter makes a "decision" that determines whether a given cluster represents a unique seismic facies, if it should be lumped in other clusters having a somewhat similar attribute expression, or whether it should be further subdivided, perhaps through the introduction of additional attributes.

Pattern recognition and classification of seismic features is fundamental to human based interpretation, where our job may be as "simple" as identifying and picking horizons and faults, or more advanced, such as the delineation of channels, mass transport complexes, carbonate buildups, or potential gas accumulations. The use of computer-assisted classification began soon after the development of seismic attributes in the 1970s (Balch, 1971; Taner et al., 1979), with the work by Sonneland (1983) and Justice et al. (1985) being two of the first. The k-means (Forgy, 1965; Jancey, 1966) was one of the earliest clustering algorithms developed, and it was quickly applied by service companies, and today it is common to almost all interpretation software packages. The k-means is an unsupervised learning algorithm, in that the interpreter provides no prior information other than the selection of attributes and the number of desired clusters.

Barnes and Laughlin (2002) review several unsupervised clustering techniques, including k-means, fuzzy clustering, and self-organizing maps (SOMs). Their primary finding was that the clustering algorithm used was less important than the choice of attributes used. Among the clustering algorithms, they favor SOM because there is topologically ordered mapping of the clusters with similar clusters lying adjacent to each other on a manifold and in the associated latent space. In our examples, a "manifold" is a deformed 2D surface that best fits the distribution of n attributes lying in an N-dimensional data space. The clusters are then mapped to a simpler 2D rectangular "latent" (Latin for "hidden") space, upon which the interpreter can either interactively define clusters or map the projections onto a 2D color bar. A properly chosen latent space can help to identify data properties that are otherwise difficult to observe in the original input space. Coleou et al.'s (2003) seismic "waveform classification" algorithm is implemented using SOM, where the "attributes" are seismic amplitudes that lie on a suite of 16 phantom horizon slices. Each (x, y) location in the analysis window results provides a 16D vector of amplitudes. When plotted one element after the other, the mean of each cluster in 16D space looks like a waveform. These waveforms lie along a 1D deformed string (the manifold) that lies in 16D. This 1D string is then mapped to a 1D line (the latent space), which in turn is mapped against a 1D continuous color bar. The proximity of such waveforms to each other on the manifold and latent spaces results in similar seismic facies appearing as similar colors. Coleou et al. (2003) generalize their algorithm to attributes other than seismic amplitude, constructing vectors of dip magnitude, coherence, and reflector parallelism. Strecker and Uden (2002) are perhaps the first to use 2D manifolds and 2D latent spaces with geophysical data, using multidimensional attribute volumes to form N-dimensional vectors at each seismic

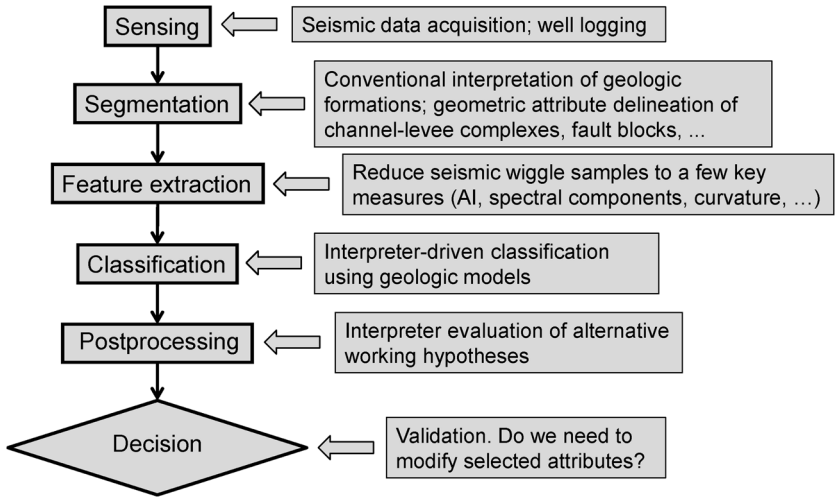

Figure 1. Classification as applied to the interpretation of seismic facies (modified from Duda et al., 2001).

sample point. Typical attributes included envelope, bandwidth, impedance, amplitude variation with offset (AVO) slope and intercept, dip magnitude, and coherence. These attributes were projected onto a 2D latent space and their results plotted against a 2D color table. Gao (2007) applies a 1D SOM to gray-level co-occurrence matrix (GLCM) texture attributes to map seismic facies offshore Angola. Overdefining the clusters with 256 prototype vectors, he then uses 3D visualization and his knowledge of the depositional environment to map the "natural" clusters. These natural clusters were then calibrated using well control, giving rise to what is called *a posteriori supervision*. Roy et al. (2013) build on these concepts and develop an SOM classification workflow of multiple seismic attributes computed over a deepwater depositional system. They calibrate the clusters a posteriori using classical principles of seismic stratigraphy on a subset of vertical slices through the seismic amplitude. A simple but very important innovation was to project the clusters onto a 2D nonlinear Sammon space (Sammon, 1969). This projection was then colored using a gradational 2D color scale like that of Matos et al. (2009), thus facilitating the interpretation. Roy et al. (2013) introduce a Euclidean distance measure to correlate predefined unsupervised clusters to average data vectors about interpreter defined well-log facies.

Generative topographic mapping (GTM) is a more recent unsupervised classification innovation, providing a probabilistic representation of the data vectors in the latent space (Bishop et al., 1998). There has been very little work on the application of the GTM technique to seismic data and exploration problems. Wallet et al. (2009) are probably the first to apply the GTM technique to seismic data, using a suite of phantom horizon slices through a seismic amplitude volume generating a waveform classification. Although generating excellent images, Roy (2013) and Roy et al. (2014) find the introduction of well control to SOM classification to be somewhat limited, and instead apply GTM to a Mississippian tripolitic chert reservoir in midcontinent USA and a carbonate wash play in the Sierra Madre Oriental of Mexico. They find that GTM provides not only the most likely cluster associated with a given voxel, but also the probability that voxel belongs each of clusters, providing a measure of confidence or risk in the prediction.

The k-means, SOM, and GTM are all unsupervised learning techniques, where the clustering is driven only by the choice of input attributes and the number of desired clusters. If we wish to teach the computer to mimic the facies identification previously chosen by a skilled interpreter, or link seismic facies to electrofacies interpreted using wireline logs, we need to introduce "supervision" or external control to the clustering algorithm. The most popular means of supervised learning classification are based on artificial neural networks (ANNs). Meldahl et al. (1999) use seismic energy and coherence attributes coupled with interpreter control (picked seed points) to train a neural network to identify hydrocarbon chimneys. West et al. (2002) use a similar workflow, in which the objective is seismic facies analysis of a channel system and the input attributes are textures. Corradi et al. (2009) use GLCM textures and ANN, with controls based on wells and skilled interpretation of some key 2D vertical slices to map sand, evaporate, and sealing versus nonsealing shale facies offshore of west Africa.

The support vector machine (SVM, where the word "machine" is due to Turing's [1950] mechanical decryption machine) is a more recent introduction (e.g., Kuzma and Rector, 2004, 2005, 2007; Li and Castagna, 2004; Zhao et al., 2005; Al-Anazi and Gates, 2010). Originating from maximum margin classifiers, SVMs have gained great popularity for solving pattern classification and regression problems since the concept of a "soft margin" was first introduced by Cortes and Vapnik (1995). SVMs map the N-dimensional input data into a higher-dimensional latent (often called *feature*) space, where clusters can be linearly separated by hyperplanes. Detailed descriptions of SVMs can be found in Cortes and Vapnik (1995), Cristianini and Shawe-Taylor (2000), and Schölkopf and Smola (2002). Li and Castagna (2004) use SVM to discriminate alternative AVO responses, whereas Zhao et al. (2014) and Zhang et al. (2015) use a variation of SVM using mineralogy logs and seismic attributes to predict lithology and brittleness in a shale resource play.

We begin our paper by providing a summary of the more common clustering techniques used in seismic facies classification, emphasizing their similarities and differences. We start from the unsupervised learning k-means algorithm, progress through projections onto principal component hyperplanes, and end with projections onto SOM and GTM manifolds, which are topological spaces that resemble Euclidean space near each point. Next, we provide a summary of supervised learning techniques including ANNs and SVMs. Given these definitions, we apply each of these methods to identify seismic facies in the same data volume acquired in the Canterbury Basin of New Zealand. We conclude with a discussion on the advantages and limitations of each method and areas for future algorithm development and workflow refinement. At the very end, we provide an appendix containing some of the mathematical details to better quantify how each algorithm works.

Review of unsupervised learning classification techniques

Crossplotting

Crossplotting one or more attributes against each other is an interactive, and perhaps the most common, clustering technique. In its simplest implementation, one computes and then displays a 2D histogram of two attributes. In most software packages, the interpreter then identifies a cluster of interest and draws a polygon around it. Although several software packages allow crossplotting of up to three attributes, crossplotting more than three attributes quickly becomes

intractable. One workflow to address this visualization limitation is to first project a high number of attributes onto the first two or three eigenvectors, and then crossplot the principal components. Principal components will be discussed later in the section on projection methods.

k-means classification

The *k*-means (MacQueen, 1967) is perhaps the simplest clustering algorithm and is widely available in commercial interpretation software packages. The method is summarized in the cartoons shown in Figure 2. One drawback of the method is that the interpreter needs to define how many clusters reside in the data. Once the number of clusters is defined, the cluster means or centers are defined either on a grid or randomly to begin the iteration loop. Because attributes have different units of measurement (e.g., Hertz for peak frequency, 1/km for curvature, and millivolt for the root-mean-square amplitude), the distance of each data point to the current means is computed by scaling the data by the inverse of the covariance matrix, giving us the "Mahalanobis distance" (see Appendix A). Each data point is then assigned to the cluster to whose mean it is closest. Once assigned, new cluster means are computed from the newly assigned data clusters and the process is repeated. If there are Q clusters, the process will converge in about Q iterations.

The *k*-means is fast and easy to implement. Unfortunately, the clustering has no structure, such that there is no relationship between the cluster numbering (and therefore coloring) and the proximity of one cluster to another. This lack of organization can result in similar facies appearing in totally different colors, confusing the interpretation. Tuning the number of clusters to force similar facies into the same cluster is a somewhat tedious procedure that also decreases the resolution of the facies map.

Projection techniques

Although not defined this way in the pattern recognition literature because this is a tutorial, we will lump the following methods, principal component analysis (PCA), SOM, and generative topographic maps, together and call them *projection techniques*. Projection techniques project data residing in a higher-dimensional space (for example, a 5D space defined by five attributes) onto a lower dimensional space (for example, a 2D plane or deformed 2D surface). Once projected, the data can be clustered in that space by the algorithm (such as SOM) or interactively clustered by the interpreter by drawing polygons (routine for PCA, and our preferred analysis technique for SOM and GTM).

Principal component analysis

PCA is widely used to reduce the redundancy and excess dimensionality of the input attribute data. Such reduction is based on the assumption that most of the signals are preserved in the first few principal components (eigenvectors), whereas the last principal components contain uncorrelated noise. In this tutorial, we will use PCA as the first iteration of the SOM and GTM algorithms. Many workers use PCA to reduce redundant attributes into "meta attributes" to simplify the computation. The first eigenvector is a vector in N-dimensional attribute space that best represents the attribute patterns in the data. Crosscorrelating (projecting) the N-dimensional data against the first eigenvector at each voxel gives us the first principal component volume. If we scale the first eigenvector by the first principal component and subtract it from the original data vector, we obtain a residual data vector. The second eigenvector is that vector that best represents the attribute patterns in this residual. Crosscorrelating (projecting) the second eigenvector against either the original data or residual data vector at each voxel gives us the second principal component volume. This process continues for all N-dimensions resulting in N eigen-

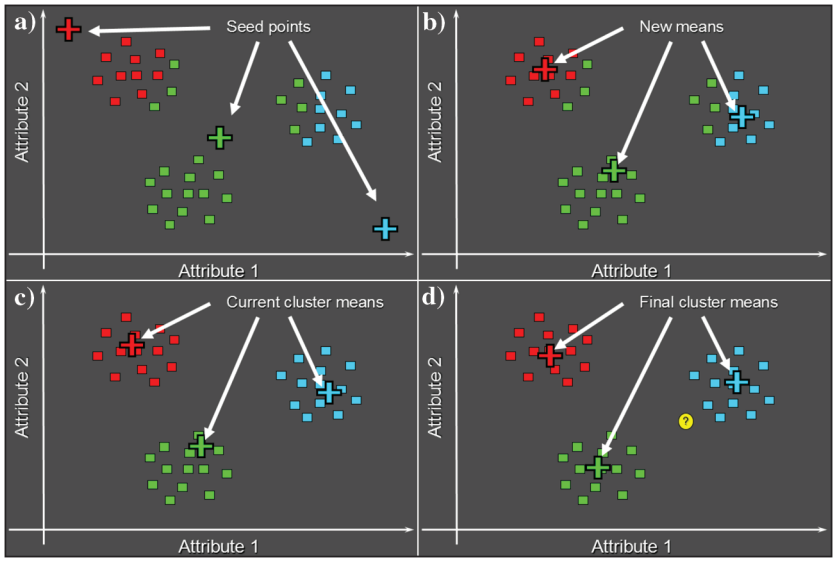

Figure 2. Cartoon illustration of a *k*-means classification of three clusters. (a) Select three random or equally spaced, but distinct, seed points, which serve as the initial estimate of the vector means of each cluster. Next, compute the Mahalanobis distance between each data vector and each cluster mean. Then, color code or otherwise label each data vector to belong to the cluster that has the smallest Mahalanobis distance. (b) Recompute the means of each cluster from the previously defined data vectors. (c) Recalculate the Mahalanobis distance from each vector to the new cluster means. Assign each vector to the cluster that has the smallest distance. (d) The process continues until the changes in means converge to their final locations. If we now add a new (yellow) point, we will use a Bayesian classifier to determine into which cluster it falls (figure courtesy S. Pickford).

vectors and N principal components. In this paper, we will limit ourselves to the first two eigenvectors, which thus define the plane that least-squares fits the N-dimensional attribute data. Figure 3c shows a numerical example of the first two principal components defining a plane in a 3D data space.

Self-organizing maps

Although many workers (e.g., Coleou et al., 2003) describe the SOM as a type of neural network, for the purposes of this tutorial, we prefer to describe the SOM as a manifold projection technique Kohonen (1982). SOM, originally developed for gene pattern recognition, is one of the most popular classification techniques, and it has been implemented in at least four commercial software packages for seismic facies classification. The major advantage of SOM over k-means is that the clusters residing on the deformed manifold in N-dimensional data space are directly mapped to a rectilinear or otherwise regularly gridded latent space. We provide a brief summary of the mathematical formulations of the SOM implementation used in this study in Appendix A.

Although SOM is one of the most popular classification techniques, there are several limitations to the SOM algorithm. First, the choice of neighborhood function at each iteration is subjective, with different choices resulting in different solutions. Second, the absence of a quantitative error measure does not let us know whether the solution has converged to an acceptable level, thus providing confidence in the resulting analysis. Third, although we find the most likely cluster for a given data vector, we have no quantitative measure of confidence in the facies classification, and no indication if the vector could be nearly as well represented by other facies.

Generative topographic mapping

GTM is a nonlinear dimensionality reduction technique that provides a probabilistic representation of the data vectors on a lower L-dimensional deformed manifold that is in turn mapped to an L-dimensional latent space. Although SOM seeks the node or prototype vector that is closest to the randomly chosen vector from the training or input data set, in GTM, each of the nodes lying on the lower dimensional manifold provides some mathematical support to the data and is considered to be to some degree "responsible" for the data vector (Figure 4). The level of support or "responsibility" is modeled with a constrained mixture of Gaussians. The model parameter estimations are determined by maximum likelihood using the expectation maximization (EM) algorithm (Bishop et al., 1998).

Because GTM theory is deeply rooted in probability, it can also be used in modern risk analysis. We can extend the GTM application in seismic exploration by projecting the mean posterior probabilities of a particular window of multiattribute data (i.e., a producing well) onto the 2D latent space. By project the data vector at any given voxel onto the latent space, we obtain a probability estimates of whether it falls into the same category (Roy et al., 2014). We thus have a probabilistic estimate of how similar any data vector is to attribute behavior (and hence facies) about a producing or nonproducing well of interest.

Other unsupervised learning methods

There are many other unsupervised learning techniques, several of which were evaluated by Barnes and Laughlin (2002). We do not currently have access to software to apply independent component analysis (ICA) and Gaussian mixture models (GMMs) to our

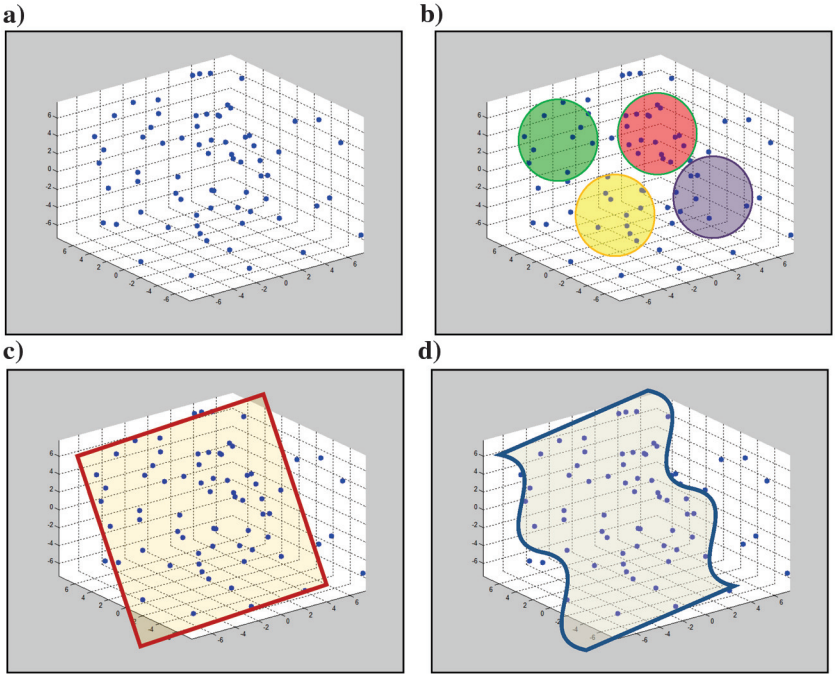

Figure 3. (a) A distribution of data points in 3D attribute space. The statistics of this distribution can be defined by the covariance matrix. (b) k-means will cluster data into a user-defined number of distributions (four in this example) based on the Mahalanobis distance measure. (c) The plane that best fits these data is defined by the first two eigenvectors of the covariance matrix. The projection of the 3D data onto this plane provides the first two principal components of the data, as well as the initial model for our SOM and GTM algorithms. (d) SOM and GTM deform the initial 2D plane into a 2D manifold that better fits the data. Each point on the deformed 2D manifold is in turn mapped to a 2D rectangular latent space. Clusters are color coded or interactively defined on this latent space.

seismic facies classification problem, but we mention them as possible candidates.

Independent component analysis

Like PCA, ICA is a statistical technique used to project a set of N-dimensional vectors onto a smaller L-dimensional space. Unlike PCA, which is based on Gaussian statistics, whereby the first eigenvector best represents the variance in the multidimensional data, ICA attempts to project data onto subspaces that result in non-Gaussian distributions, which are then easier to separate and visualize. Honório et al. (2014) successfully apply ICA to multiple spectral components to delineate the architectural elements of an offshore Brazil carbonate terrain. PCA and ICA are commonly used to reduce a redundant set of attributes to form a smaller set of independent meta-attributes (e.g., Gao, 2007).

Gaussian mixture models

GMMs are parametric models of probability distributions, which can provide greater flexibility and precision in modeling than traditional unsupervised clustering algorithms. Lubo et al. (2014) apply this technique to a suite of well logs acquired over Horseshoe Atoll, west Texas, to generate different lithologies. These GMM lithologies are then used to calibrate 3D seismic prestack inversion results to generate a 3D rock property model. At present, we do not know of any GMM algorithms applied to seismic facies classification using seismic attributes as input data.

Review of supervised learning classification techniques

Artificial neural networks

ANNs can be used in unsupervised and supervised mulitattribute analysis (van der Baan and Jutten, 2000). The multilayer perceptron and the radial basis function (RBF) are two popular types of neural networks used in supervised learning. The probabilistic neural network (PNN), which also uses RBF, forms the basis of additional neural network geophysical applications. In terms of network architecture, the supervised algorithms are feed-forward networks. In contrast, the unsupervised SOM algorithm described earlier is a recurrent (or feed-backward) network. An advantage of feed-forward networks over SOMs is the ability to predict both continuous values (such as porosity), as well as discrete values (such as the facies class number). Applications of neural networks can be found in seismic inversion (Röth and Tarantola, 1994), well-log prediction from other logs (Huang et al., 1996; Lim, 2005), waveform recognition (Murat and Rudman, 1992), seismic facies analysis (West et al., 2002), and reservoir property prediction using seismic attributes (Yu et al., 2008; Zhao and Ramachandran, 2013). For the last application listed above, however, due to the

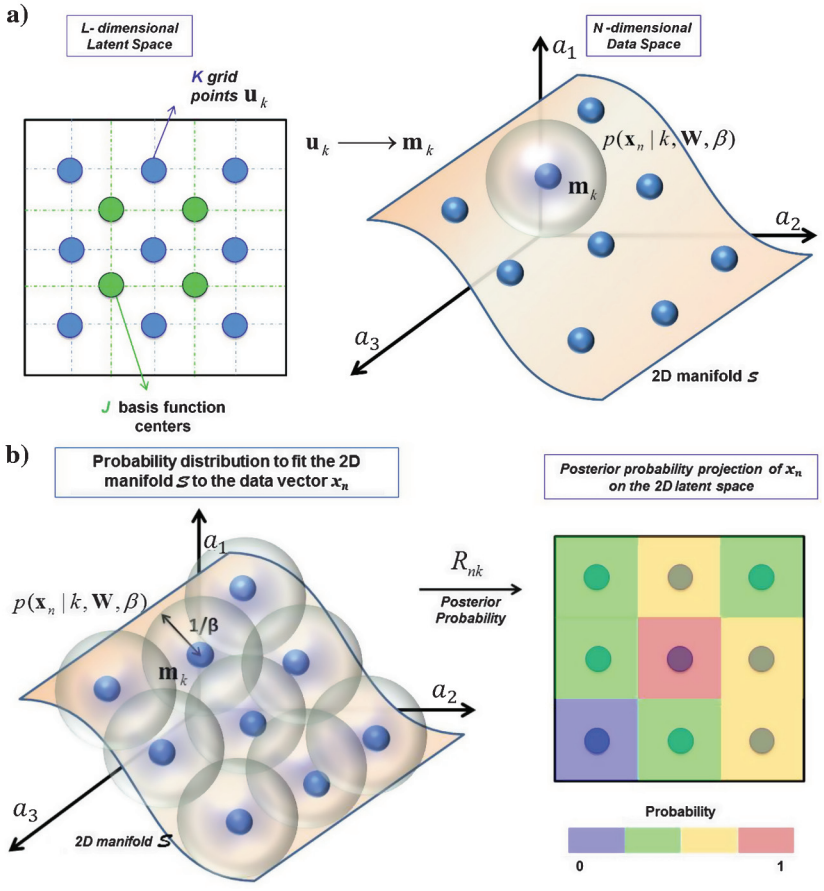

Figure 4. (a) The K grid points $\mathbf{u}_k$ defined on a L-dimensional latent space grid are mapped to K grid points $\mathbf{m}_k$ lying on a non-Euclidean manifold in N-dimensional data space. In this paper, $L = 2$, and it will be mapped against a 2D color bar. The Gaussian mapping functions are initialized to be equally spaced on the plane defined by the first two eigenvectors. (b) Schematic showing the training of the latent space grid points to a data vector $\mathbf{a}_j$ lying near the GTM manifold using an EM algorithm. The posterior probability of each data vector is calculated for all Gaussian centroids points $\mathbf{m}_k$ and are assigned to the respective latent space grid points $\mathbf{u}_k$. Grid points with high probabilities are displayed as bright colors. All variables are discussed in Appendix A.

resolution difference between seismic and well logs, structural and lithologic variation of interwell points, and the highly nonlinear relation between these two domains, achieving a convincing prediction result can be challenging. In this case, geostatistical methods, such as Bayesian analysis, can be used jointly to provide a probability index, giving interpreters an estimate of how much confidence they should have in the prediction.

ANNs are routinely used in the exploration and production industry. ANN provides a means to correlate well measurements, such as gamma-ray logs to seismic attributes (e.g., Verma et al., 2012), where the underlying relationship is a function of rock properties, the depositional environment, and diagenetic alteration. Although it has produced reliable classification in many applications during its service, defects such as converging to local minima and difficult in parameterization are not negligible. In industrial and scientific applications, we prefer a constant and robust classifier, once the training vectors and model parameters have been determined. This leads to the more recent supervised learning technique developed in the late 20th century, the SVM.

Support vector machines

The basic idea of SVMs is straightforward. First, we transform the training data vectors into a still higher-dimensional "feature" space using nonlinear mapping. Then, we find a hyperplane in this feature space that separates the data into two classes with an optimal "margin." The concept of a margin is defined to be the smallest distance between the separation hyperplane (commonly called a *decision boundary*) and the training vectors (Bishop, 2006) (Figure 5). An optimal margin balances two criteria: maximizing the margin, thereby giving the classifier the best generalization and minimizing the number of misclassified training vectors if the training data are not linearly separable. The margin can also be described as the distance between the decision boundary and two hyperplanes defined by the data vectors, which have the smallest distance to the decision boundary. These two hyperplanes are called the *plus plane* and the *minus plane*. The vectors that lie exactly on these two hyperplanes mathematically define or "support" them and are called *support vectors*. Tong and Koller (2001) show that the decision boundary is dependent solely on the support vectors, resulting in the name SVMs.

SVMs can be used in either a supervised or in a semisupervised learning mode. In contrast to supervised learning, semisupervised learning defines a learning process that uses labeled and unlabeled vectors. When there are a limited number of interpreter classified data vectors, the classifier may not act well due to insufficient training. In semisupervised training, some of the nearby unclassified data vectors are automatically selected and classified based on a distance measurement during the training step, as in an unsupervised learning process. These vectors are then used as additional training vectors (Figure 6), resulting in a classifier that will perform better for the specific problem. The generalization power is sacrificed by using unlabeled data. In this tutorial, we focus on SVM; however, the future of semisupervised SVM in geophysical applications is quite promising.

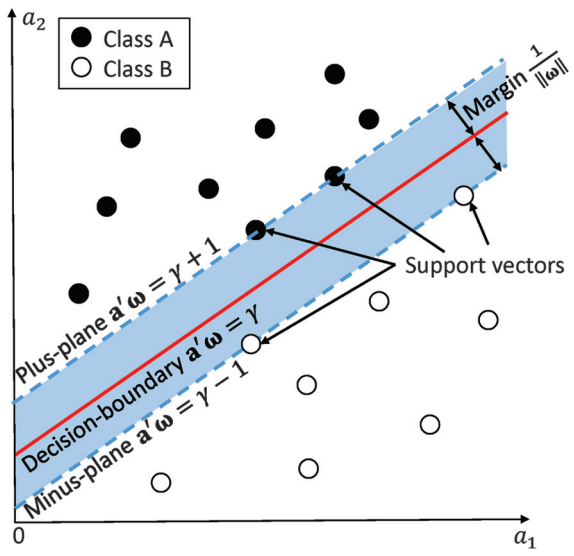

Figure 5. Cartoon of a linear SVM classifier separating black from white data vectors. The two dashed lines are the margins defined by the support vector data points. The red decision boundary falls midway between the margins, separating the two clusters. If the data clusters overlap, no margins can be drawn. In this situation, the data vectors will be mapped to a higher-dimensional space, where they can be separated.

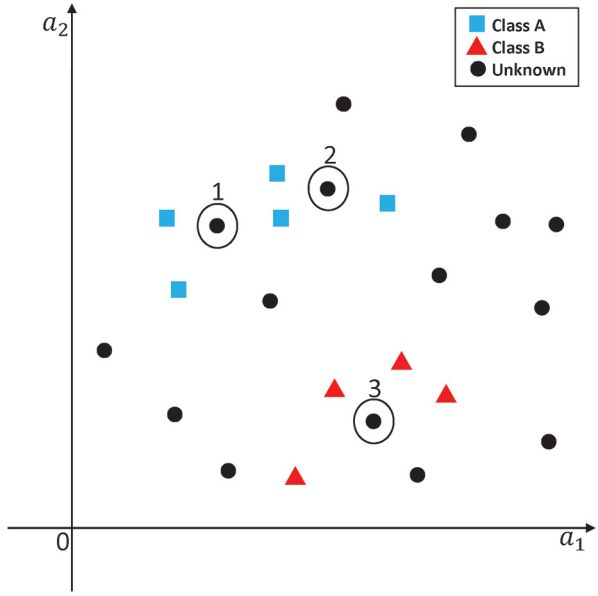

Figure 6. Cartoon describing semisupervised learning. Blue squares and red triangles indicate two different interpreter-defined classes. Black dots indicate unclassified points. In semisupervised learning, unclassified data vectors 1 and 2 are classified to be class "A," whereas data vector 3 is classified to be class "B" during the training process.

Proximal support vector machines

The proximal support vector machine (PSVM) (Fung and Mangasarian, 2001, 2005) is a recent variant of SVM, which, instead of looking for a separating plane directly, builds two parallel planes that approximate two data classes; the decision-boundary then falls between these two planes (Figure 7). Other researchers have found that PSVM provides comparable classification correctness with standard SVM but at considerable computational savings (Fung and Mangasarian, 2001, 2005; Mangasarian and Wild, 2006). In this tutorial, we use PSVM as our implementation of SVM. Details on the PSVM algorithm are provided in Appendix A.

We may face problems in seismic interpretation that are linearly inseparable in the original input multidimensional attribute space. In SVM, we map the data vectors into a higher-dimensional space where they become linearly separable (Figure 8), where the increase in dimensionality may result in significantly increased computational cost. Instead of using an explicit mapping function to map input data into a higher-dimensional space, PSVM achieves the same goal by manipulating a kernel function in the input attribute space. In our implementation, we use a Gaussian kernel function, but in principle, many other functions can be used (Shawe-Taylor and Cristianini, 2004).

SVM can be used either as a classifier or as a regression operator. Used as a regression operator, SVM is capable of predicting petrophysical properties, such as porosity (Wong et al., 2005), V_P, V_S, and density (Kuzma and Rector, 2004), as well as permeability (Al-Anazi and Gates, 2010; Nazari et al., 2011). In all such applications, SVM shows comparable or superior performance with neural networks with respect to prediction error and training cost. When used as a classifier, SVM is suitable in predicting lithofacies (Al-Anazi and Gates, 2010; Torres and Reveron, 2013; Wang et al., 2014; Zhao et al., 2014) or pseudo rock properties (Zhang et al., 2015), either from well-log data, core data, or seismic attributes.

Geologic setting

In this tutorial, we used the Waka 3D seismic survey acquired over the Canterbury Basin, offshore New Zealand, generously made public by New Zealand Petroleum and Minerals. Readers can request this data set through their website for research purposes. Figure 9 shows the location of this survey, where the red rectangle corresponds to time slices shown in subsequent figures. The study area lies on the transition zone of continental slope and rise, with abundance of paleocanyons and turbidite deposits of Cretaceous and Tertiary ages. These sediments are deposited in a single, tectonically driven transgressive-regressive cycle (Uruski, 2010). Being a very recent and underexplored prospect, publicly available comprehensive studies of the Canterbury Basin are somewhat limited. The modern seafloor canyons shown in Figure 9 are good analogs of the deeper paleocanyons illuminated by the 3D seismic amplitude and attribute data.

Attribute selection

In their comparison of alternative unsupervised learning techniques, Barnes and Laughlin (2002) con-

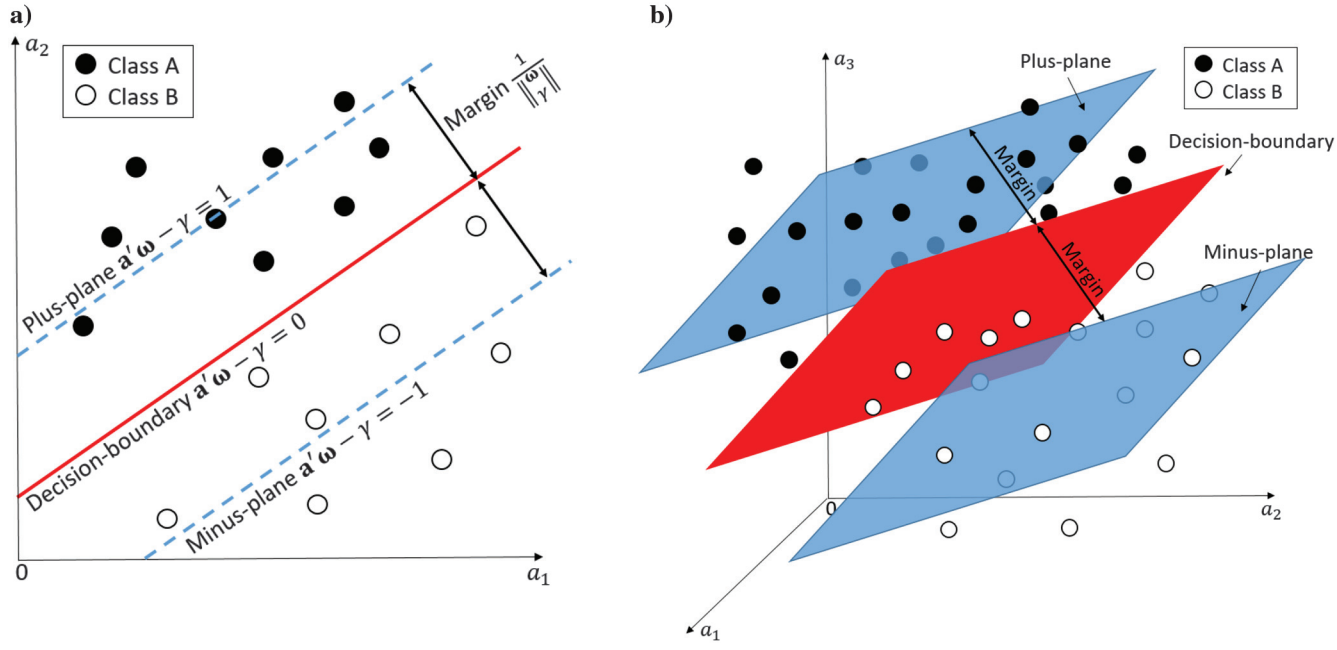

Figure 7. (a) Cartoon showing a two-class PSVM in 2D space. Classes A and B are approximated by two parallel lines that have been pushed as far apart as possible forming the cluster "margins." The red decision-boundary lies midway between the two margins. Maximizing the margin is equivalent to minimizing $(\omega^T\omega + \gamma^2)^{\frac{1}{2}}$. (b) A two-class PSVM in 3D space. In this case, the decision-boundary and margins are 2D planes.

clude that the appropriate choice of attributes was the most critical component of computer-assisted seismic facies identification. Although interpreters are skilled at identifying facies, such recognition is often subconscious and hard to define (see Eagleman's [2012] discussion on differentiating male from female chicks and identifying military aircraft from silhouettes). In supervised learning, the software does some of the work during the training process, although we must always be wary of false correlations, if we provide too many attributes (Kalkomey, 1997). For the prediction of continuous data, such as porosity, Russell (1997) suggests that one begin with exploratory data analysis, where one crosscorrelates a candidate attribute with the desired property at the well. Such crosscorrelation does not work well when trying to identify seismic facies,

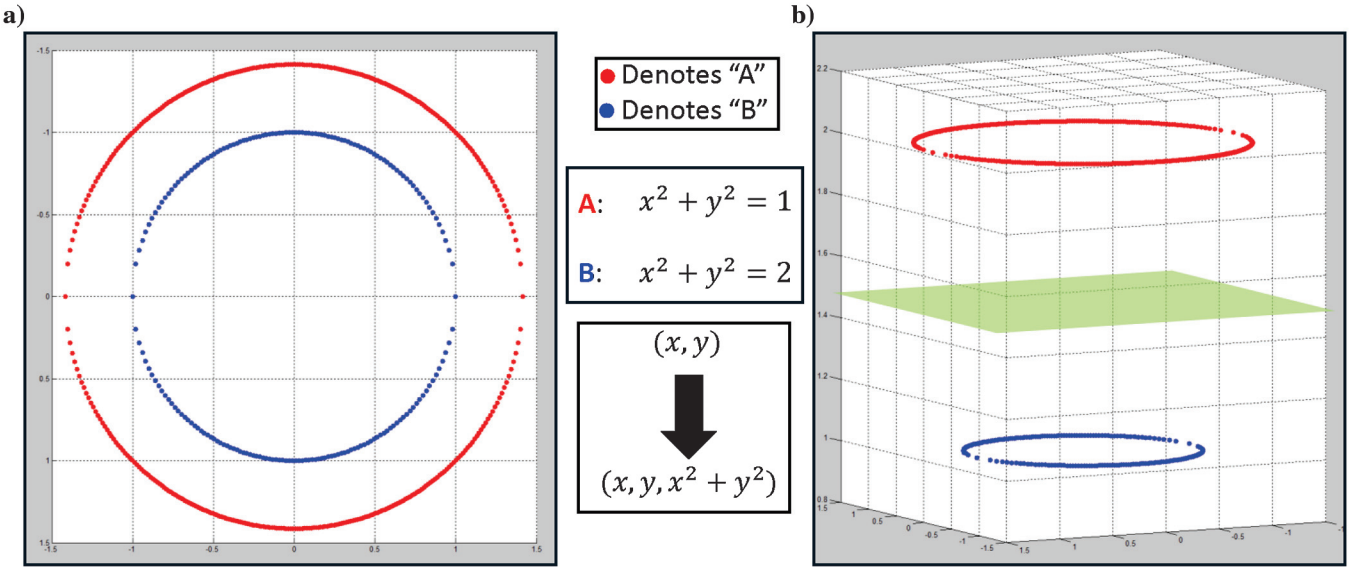

Figure 8. Cartoon showing how one SVM can map two linearly inseparable problem into a higher-dimensional space, in which they can be separated. (a) Circular classes A and B in a 2D space cannot be separated by a linear decision-boundary (line). (b) Mapping the same data into a higher 3D feature space using the given projection. This transformation allows the two classes to be separated by the green plane.

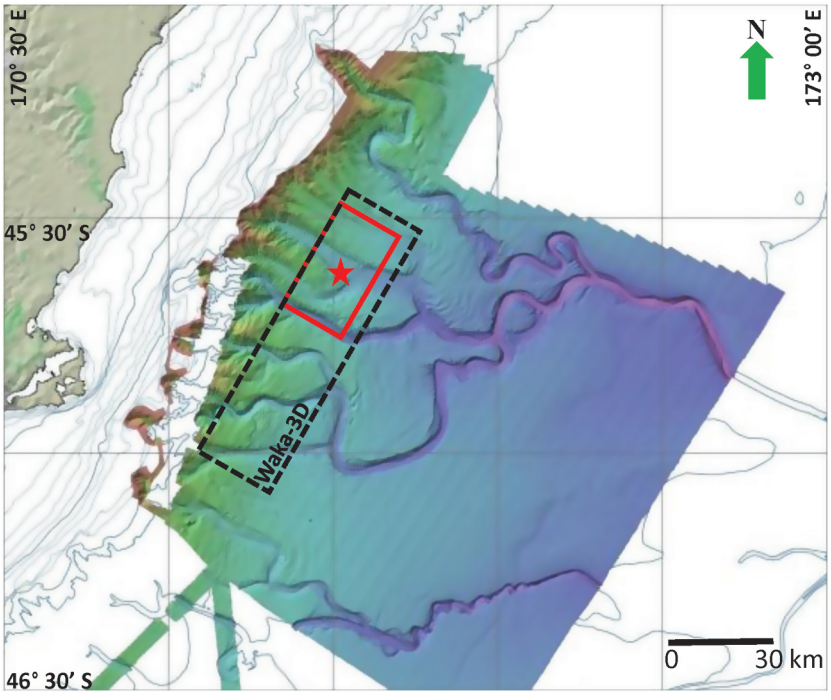

Figure 9. A map showing the location of the 3D seismic survey acquired over the Canterbury Basin, offshore New Zealand. The black rectangle denotes the limits of the Waka 3D survey, whereas the smaller red rectangle denotes the part of the survey shown in subsequent figures. The colors represent the relative depth of the current seafloor, warm being shallower, and cold being deeper. Current seafloor canyons are delineated in this map, which are good analogs for the paleocanyons in Cretaceous and Tertiary ages (modified from Mitchell and Neil, 2012).

Table 1. Attribute expressions of seismic facies.

Facies	Appearance to interpreter	Attribute expression
Levee	Structurally high	Stronger dome- or ridge-shaped structural components
	Locally continuous	Higher GLCM homogeneity and lower GLCM entropy
	Higher amplitude	Dome- or ridge-shaped component
	Possibly thicker	Lower peak spectral frequency
Channel thalwegs	Shale filled with negative compaction	Stronger bowl- or valley-shaped structural components and higher peak spectral frequency
	Sand filled with positive compaction	Stronger dome- or ridge-shaped structural components and lower peak spectral frequency
Channel flanks	Onlap onto incisement and canyon edges	Higher reflector convergence magnitude
Gas-charged sands	High amplitude and continuous reflections	Higher GLCM homogeneity, lower GLCM entropy, and high peak magnitude
Incised floodplain	Erosional truncation	Higher reflector convergence magnitude and higher curvedness
Floodplain	Lower amplitude	Lower spectral magnitude
	Higher frequency	Higher peak spectral frequency
	Continuous	Higher GLCM homogeneity and lower GLCM entropy
	Near-planar events	Lower amplitude structural shape components and lower reflector convergence magnitude
Slumps	Chaotic reflectivity	Higher reflector convergence magnitude, higher spectral frequency, lower GLCM homogeneity, and higher GLCM entropy

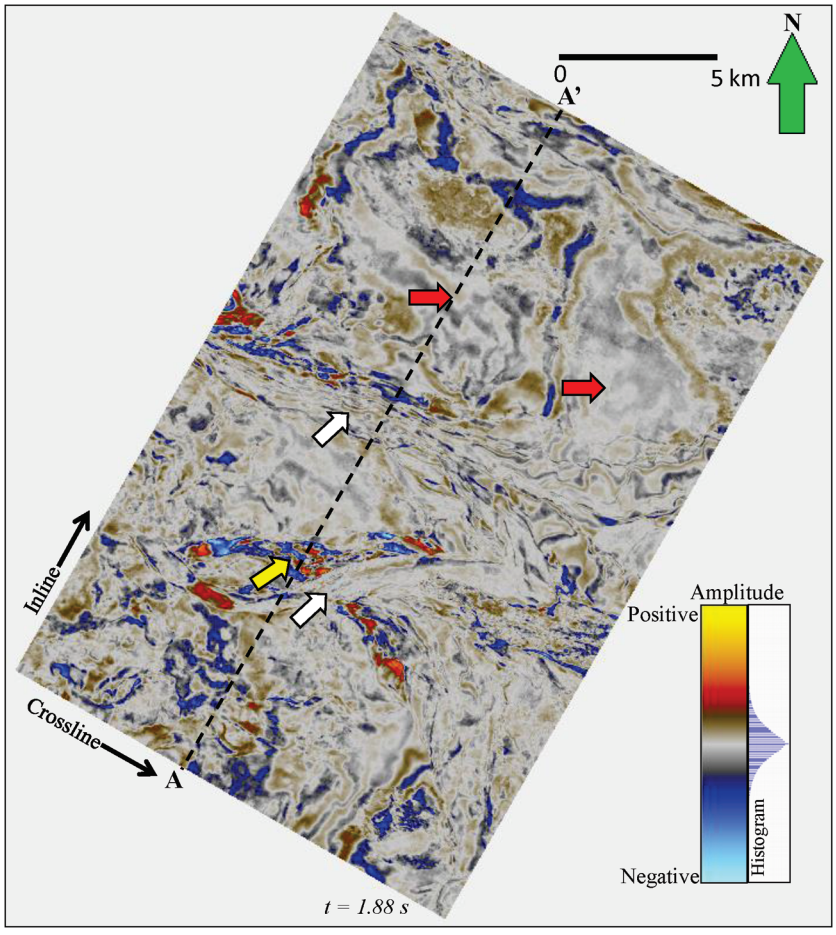

Figure 10. Time slice at $t = 1.88$ s through the seismic amplitude volume. White arrows indicate potential channel/canyon features. The yellow arrow indicates a high-amplitude feature. Red arrows indicate a relatively low-energy, gently dipping area. AA′ denotes the cross section shown in Figure 14.

which are labeled with an integer number or alphanumeric name.

Table 1 summarizes how we four interpreters perceive each of the seismic facies of interest. Once we enumerate the seismic expression, the quantification using attribute expression is relatively straightforward. In general, amplitude and frequency attributes are lithology indicators and may provide direct hydrocarbon detection in conventional reservoirs: Geometric attributes delineate reflector morphology, such as dip, curvature, rotation, and convergence, whereas statistical and texture attributes provide information about data distribution that quantifies subtle patterns that are hard to define (Chopra and Marfurt, 2007). Attributes such as coherence provide images of the edges of seismic facies rather than a measure of the facies themselves, although slumps often appear as a suite of closely spaced faults separating rotated fault blocks. Finally, what we see as interpreters and what our clustering algorithms see can be quite different. Although we may see a slump feature as exhibiting a high number of faults per kilometer, our clustering algorithms are applied voxel by voxel and see only the local behavior. Extending the clustering to see such large-scale textures requires the development of new texture attributes.

The number of attributes should be as small as possible to discriminate the facies of interest, and each attribute should be mathematically independent from the others. Although it may be fairly easy to represent three attributes with a deformed 2D manifold, increasing the dimensionality results in increased deformation, such that our manifold may fold on itself or may not accurately represent the increased data variability. Because the Waka 3D survey is new to all four authors, we test numerous attributes that we think may highlight different facies in the turbidite system. Among these attributes, we find the shape index to be good for visual classification, but it dominates the unsupervised classifications with valley and ridge features across the survey. After such analysis, we chose four attributes that are mathematically independent but should be coupled through the underlying geology, peak spectral frequency, peak spectral magnitude, GLCM homogeneity, and curvedness, as the input to our classifiers. The peak spectral frequency and peak spectral magnitude form an attribute pair that crudely represents the spectral response. The peak frequency of spectrally whitened data is sensitive to tuning thickness, whereas the peak magnitude is a function of the tuning thickness and the impedance contrast. GLCM homogeneity is a texture attribute that has a high value for adjacent traces with

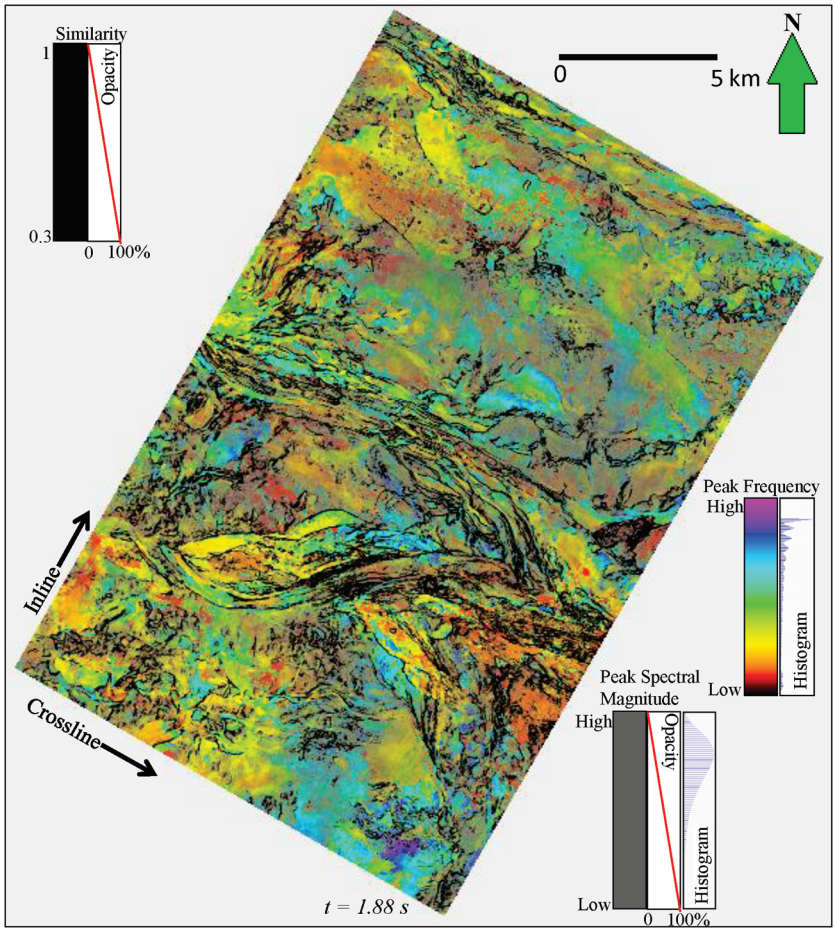

Figure 11. Time slice at $t = 1.88$ s through peak spectral frequency corendered with peak spectral magnitude that emphasizes the relative thickness and reflectivity of the turbidite system and surrounding slope fan sediments into which it was incised. The two attributes are computed using a continuous wavelet transform algorithm. The edges of the channels are delineated by Sobel filter similarity.

similar (high or low) amplitudes and measures the continuity of a seismic facies. Curvedness defines the magnitude of reflector structural or stratigraphic deformation, with dome-, ridge-, saddle-, valley-, and bowl-shaped features exhibiting high curvedness and planar features exhibiting zero curvedness.

Figure 10 shows a time slice at $t = 1.88$ s through the seismic amplitude volume, on which we identify channels (white arrows), high-amplitude deposits (yellow arrows), and slope fans (red arrows). Figure 11 shows an equivalent time slice through the peak spectral frequency corendered with the peak spectral magnitude that emphasizes the relative thickness and reflectivity of the turbidite system, as well as surrounding slope fan sediments into which it was incised. The edges of the channels are delineated by Sobel filter similarity. We show equivalent time slices through (Figure 12) GLCM homogeneity, and (Figure 13) corendered shape index and curvedness. In Figure 14, we show a representative vertical slice at line AA′ in Figure 10 cutting through the channels through (Figure 14a) seismic amplitude, (Figure 14b) seismic amplitude corendered with peak spectral magnitude/peak spectral frequency, (Figure 14c) seismic amplitude corendered with GLCM homogeneity, and (Figure 14d) seismic amplitude corendered shape index and curvedness. White arrows indicate incised valleys, yellow arrows indicate high-amplitude deposits, and red arrows indicate a slope fan. We note that several of the incised values are visible at time slice $t = 1.88$ s.

In a conventional interpretation workflow, the geoscientist would examine each of these attribute images and integrate them within a depositional framework. Such interpretation takes time and may be impractical for extremely large data volumes. In contrast, in seismic facies classification, the computer either attempts to classify what it sees as distinct seismic facies (in unsupervised learning) or attempts to emulate the interpreter's classification made on a finite number of vertical sections, time, and/or horizon slices and apply the same classification to the full 3D volume (in supervised learning). In both cases, the interpreter needs to validate the final classification to determine if they represent seismic facies of interest. In our example, we will use Sobel filter similarity to separate the facies, and we then evaluate how they fit within our understanding of a turbidite system.

Application

Given these four attributes, we now construct 4D attribute vectors as input to the previously described

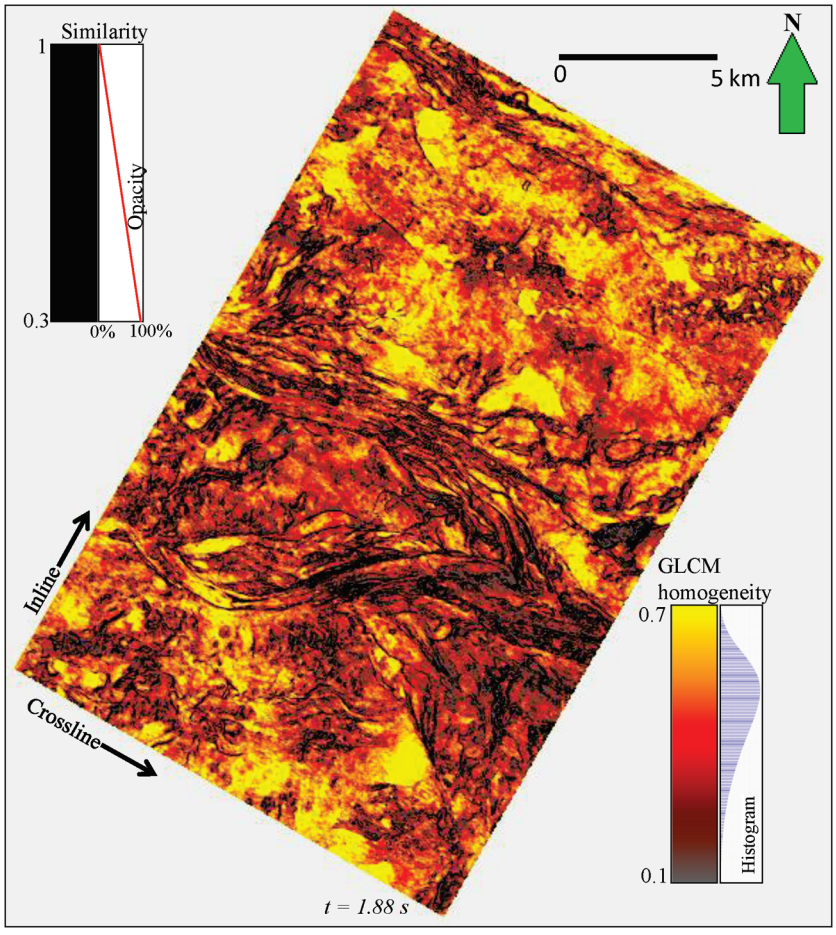

Figure 12. Time slice at $t = 1.88$ s through the GLCM homogeneity attribute corendered with Sobel filter similarity. Bright colors highlight areas with potential fan sand deposits.

classification algorithms. To better illustrate the performance of each algorithm, we summarize the data size, number of computational processors, and runtime in Table 2. All the algorithms are developed by the authors except ANN, which is implemented using the MATLAB toolbox.

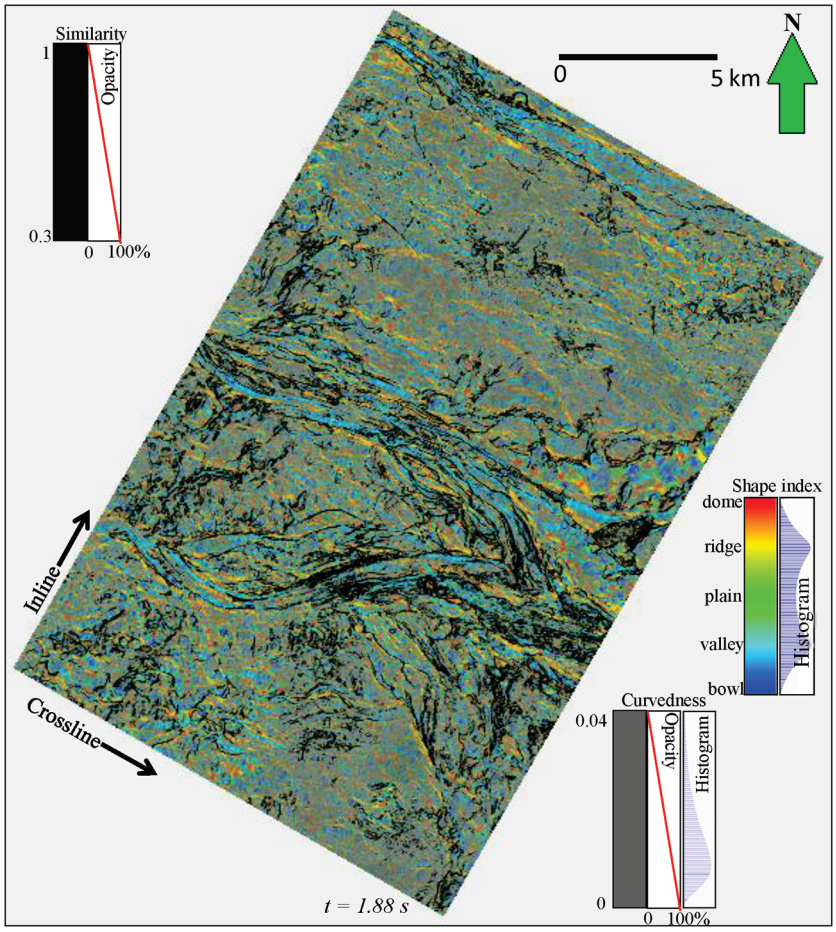

Figure 13. Time slice at $t = 1.88$ s through the corendered shape index, curvedness, and Sobel filter similarity. The shape index highlights incisement, channel flanks, and levees providing an excellent image for interactive interpreter-driven classification. However, the shape index dominates the unsupervised classifications, highlighting valley and ridge features, and minimizing more planar features of interest in the survey.

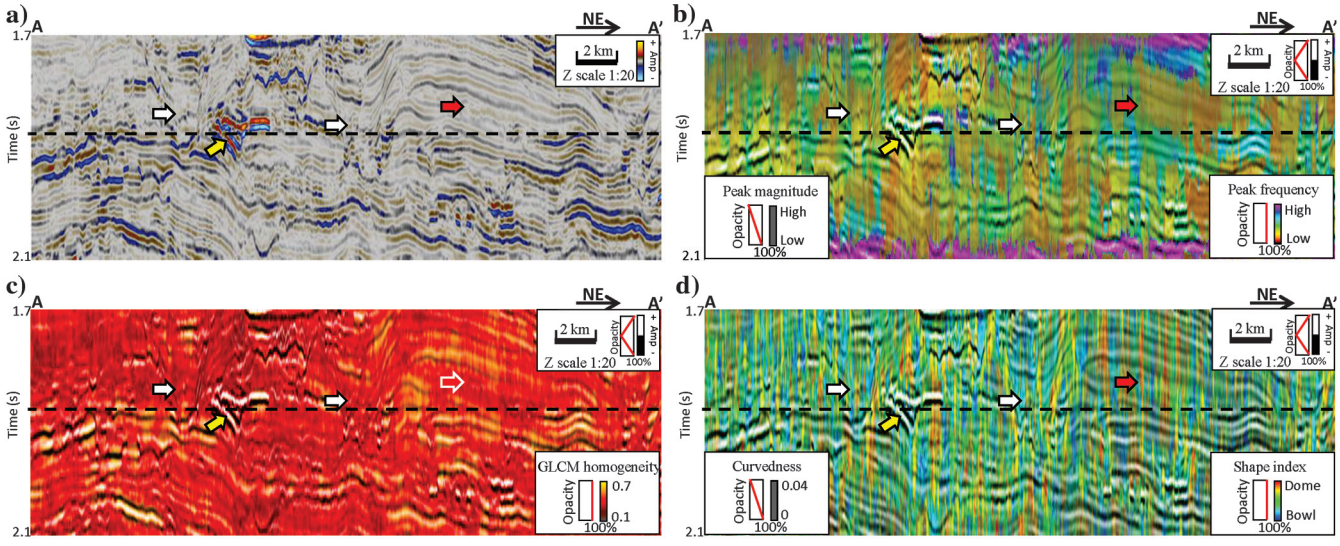

Figure 14. Vertical slices along line AA′ (location shown in Figure 10) through (a) seismic amplitude, (b) seismic amplitude corendered with peak spectral magnitude and peak spectral frequency, (c) seismic amplitude corendered with GLCM homogeneity, and (d) seismic amplitude corendered with shape index and curvedness. White arrows indicate incised channel and canyon features. The yellow arrow indicates at a high-amplitude reflector. Red arrows indicate relatively low-amplitude, gently dipping areas.

We begin with the k-means. As previously discussed, a limitation of k-means is the lack of any structure to the cluster number selection process. We illustrate this limitation by computing k-means with 16 (Figure 15) and 256 (Figure 16) clusters. On Figure 15, we can identify high-amplitude overbank deposits (yellow arrows), channels (white arrows), and slope fan deposits (red arrows). A main limitation of k-means is that there is no structure linking the clusters, which leads to a somewhat random choice of color assignment to clusters. This problem becomes more serious when more clusters are selected: The result with 256 clusters (Figure 16) is so chaotic that we can rarely separate the overbank high-amplitude deposits (yellow arrows) and slope fan deposits (red arrows) that were easily separable in Figure 15. For this reason, modern k-means

Table 2. Classification settings and runtimes.

			Data set size (samples)		Runtime (s)		
Algorithm	Number of classes	MPI processors[4]	Training	Total	Training	Applying to the entire data set	Total
k-means	16	50	809,600	101,200,000	65	20	85
k-means	256	50	809,600	101,200,000	1060	70	1130
SOM	256	1	809,600	101,200,000	4125	6035	10,160
GTM	—	50	809,600	101,200,000	9582	1025	10,607
ANN[5]	4	1	437	101,200,000	2	304	306
SVM	4	50	437	101,200,000	24	12,092	12,116

[4]SOM is not run under MPI in our implementation. ANN is run using MATLAB and is not under MPI. The other three are run under MPI when applying the model to the entire data set.
[5]ANN is implemented using the MATLAB toolbox.

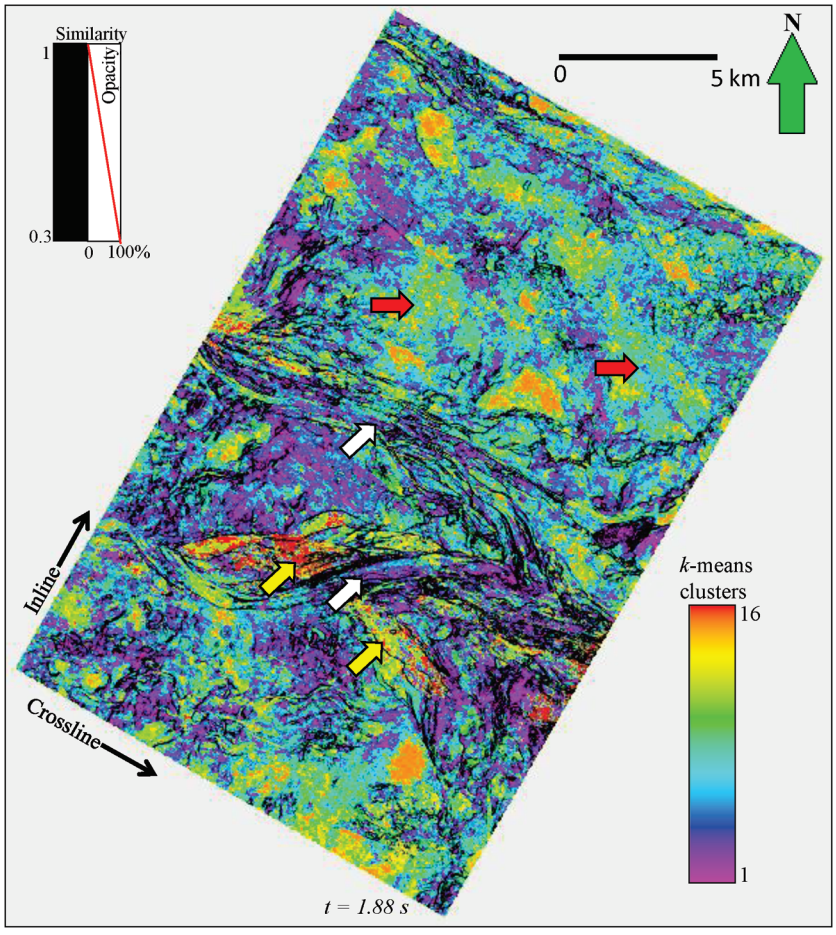

Figure 15. Time slice at $t = 1.88$ s through a k-means classification volume with $K = 16$. White arrows indicate channel-like features. Yellow arrows indicate high-amplitude overbank deposits. Red arrows indicate possible slope fans. The edges of the channels are delineated by Sobel filter similarity.

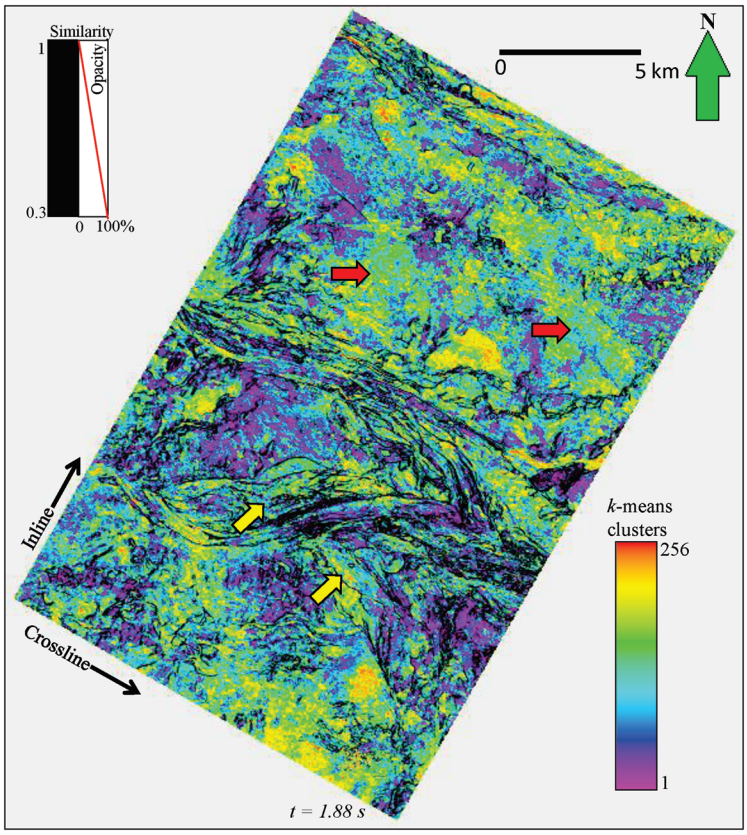

Figure 16. Time slice at $t = 1.88$ s through k-means classification volume with $K = 256$. The classification result follows the same pattern as $K = 16$, but it is more chaotic because the classes are computed independently and are not constrained to fall on a lower dimensional manifold. Note the similarity between clusters of high-amplitude overbank (yellow arrows) and slope fan deposits (red arrows), which were separable in Figure 15.

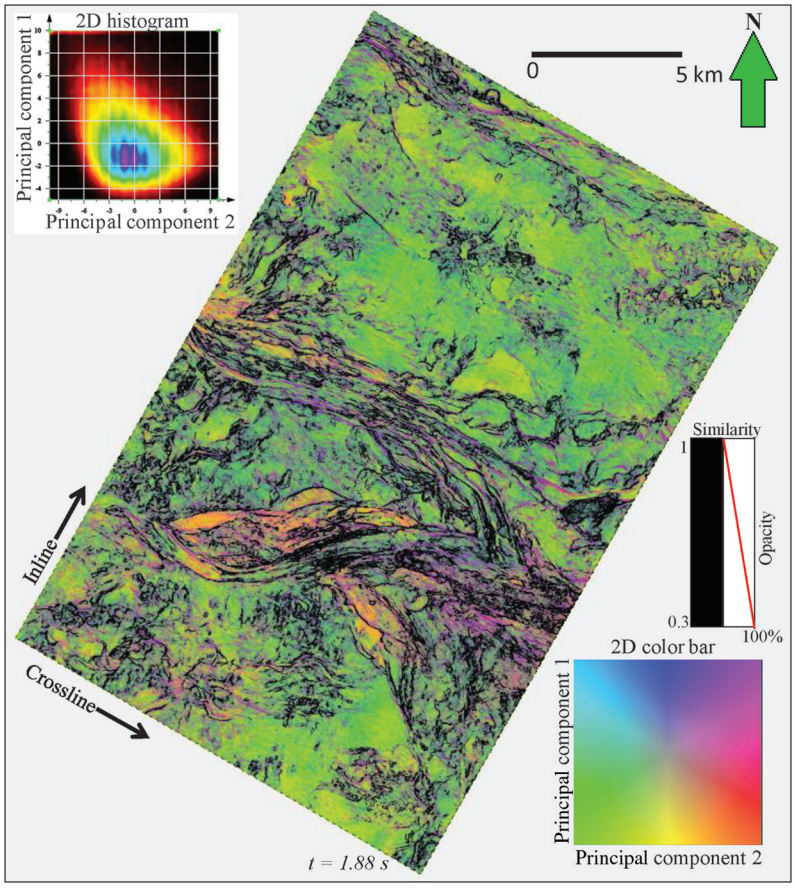

Figure 17. Time slice at $t = 1.88$ s of the first two principal components plotted against a 2D color bar. These two principal components serve as the initial model for the SOM and GTM images that follow. With each iteration, the SOM and GTM manifolds will deform to better fit the natural clusters in the input data.

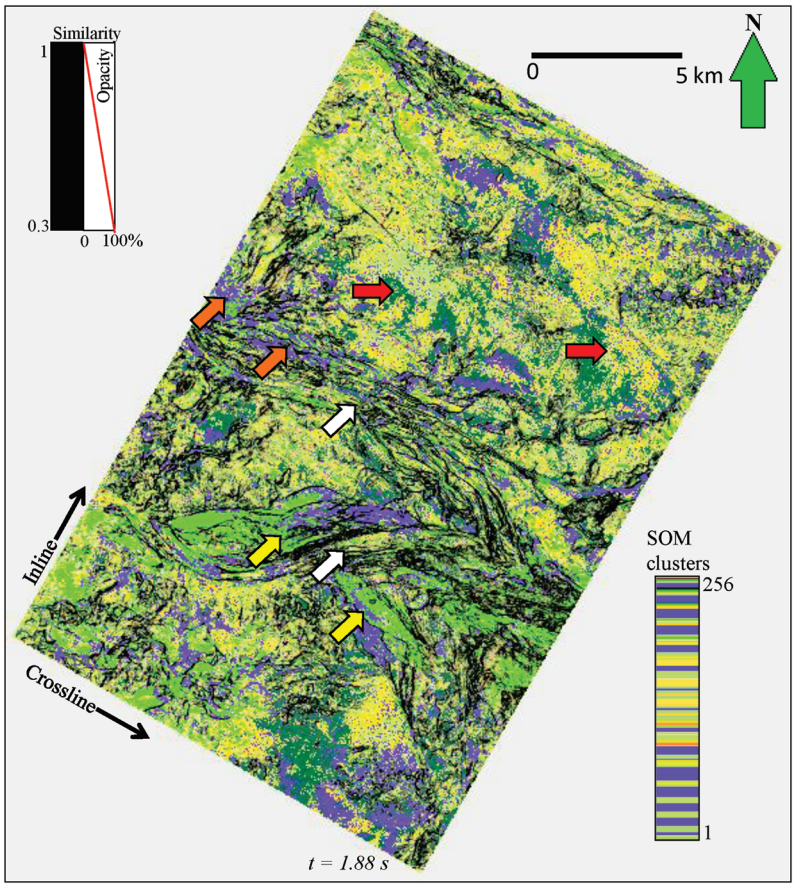

Figure 18. Time slice at $t = 1.88$ s through an SOM classification volume using 256 clusters. White arrows indicate channel-like features. Combined with vertical sections through seismic amplitude, we interpret overbank deposits (yellow arrows), crevasse splays (orange arrows), and slope fan deposits (red arrows). The data are mapped to a 2D manifold initialized by the first two principal components and are somewhat more organized than the k-means image shown in the previous figures.

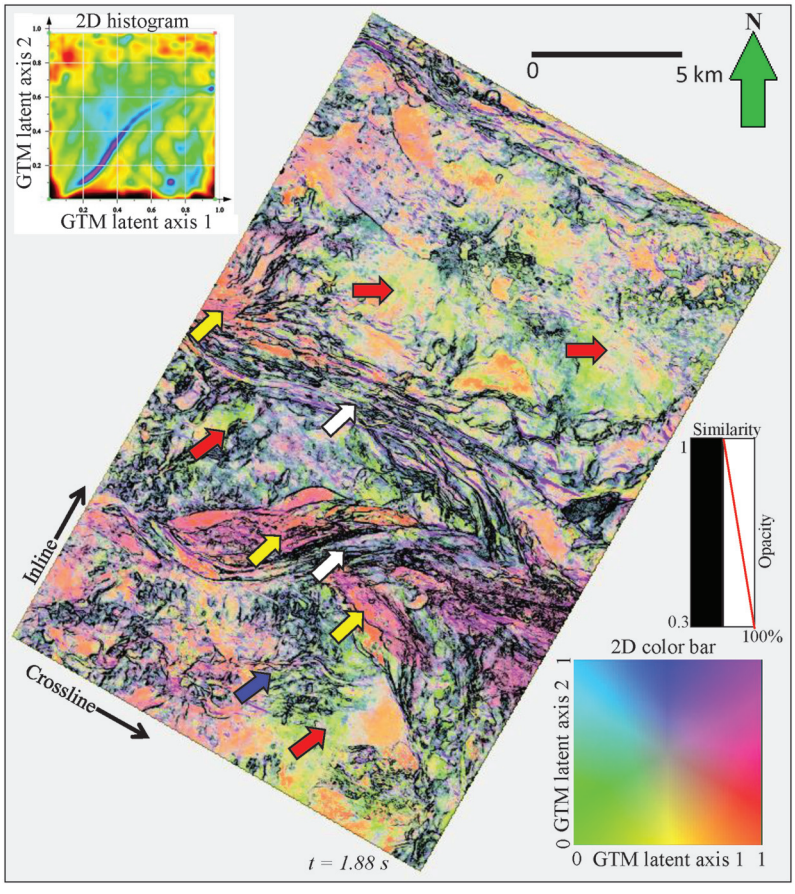

Figure 19. Time slice at $t = 1.88$ s through crossplotting GTM projections 1 and 2 using a 2D color bar. White arrows indicate channel-like features, yellow arrows indicate overbank deposits, and red arrows indicate slope fan deposits. The blue arrow indicates a braided channel system that can be seen on PCA but cannot be identified from k-means or SOM classification maps. The color indicates the location of the mean probability of each data vector mapped into the 2D latent space.

applications focus on estimating the correct number of clusters in the data.

In contrast to *k*-means, SOM restricts the cluster centers to lie on a deformed 2D manifold. Although clusters may move closer or further apart, they still form (in our implementation) a deformed quadrilateral mesh, which maps to a rectangular mesh on the 2D latent space. Mapping the latent space to a continuous 1D (Coleou et al., 2003) or 2D color bar (Strecker and Uden, 2002), reduces the sensitivity to the number of clusters chosen. We follow Gao (2007) and avoid guessing at the number of clusters necessary to represent the data by overdefining the number of prototype vectors to be 256 (the limit of color levels in our commercial display software). These 256 prototype vectors (potential clusters) reduce to only three or four distinct natural clusters through the SOM neighborhood training criteria. The 2D SOM manifold is initialized using the first two principal components, defining a plane through the *N*-dimensional attribute space (Figure 17). The algorithm then deforms the manifold to better fit the data. Overdefining the number of prototype vectors results in clumping into a smaller number natural clusters. These clumped prototype vectors project onto adjacent locations in the latent space, therefore, appear as subtle shades of the same color as indicated by the limited palette of 256 colors shown in Figure 18. On the classification result shown in Figure 18, we can clearly identify the green colored spillover deposits (yellow arrows). The difference between channel fill (white arrows) and slope fans (red arrows) is insignificant. However, by corendering with similarity, the channels are delineated nicely, allowing us to visually distinguish channel fills and the surrounded slope fans. We can also identify some purple color clusters (orange arrows), which we interpret to be crevasse splays.

Next, we apply GTM to the same four attributes. We compute two "orthogonal" projections of data onto the manifold and then onto the two dimensions of the latent space. Rather than define explicit clusters, we project the mean a posteriori probability distribution onto the 2D latent space and then export the projection onto the two latent space axes. We crossplot the projections along axes 1 and 2 and map them against a 2D color bar (Figure 19). In this slice, we see channels delineated by purple colors (white arrows), point bar and crevasse splays in pinkish colors (yellow arrows), and slope fans in lime green colors (red arrows). We can also identify some thin, braided channels at the south end of the survey (blue arrow). Similarly to the SOM result, similarity separates the incised valleys from the slope fans. However, the geologic meaning of the orange-colored facies

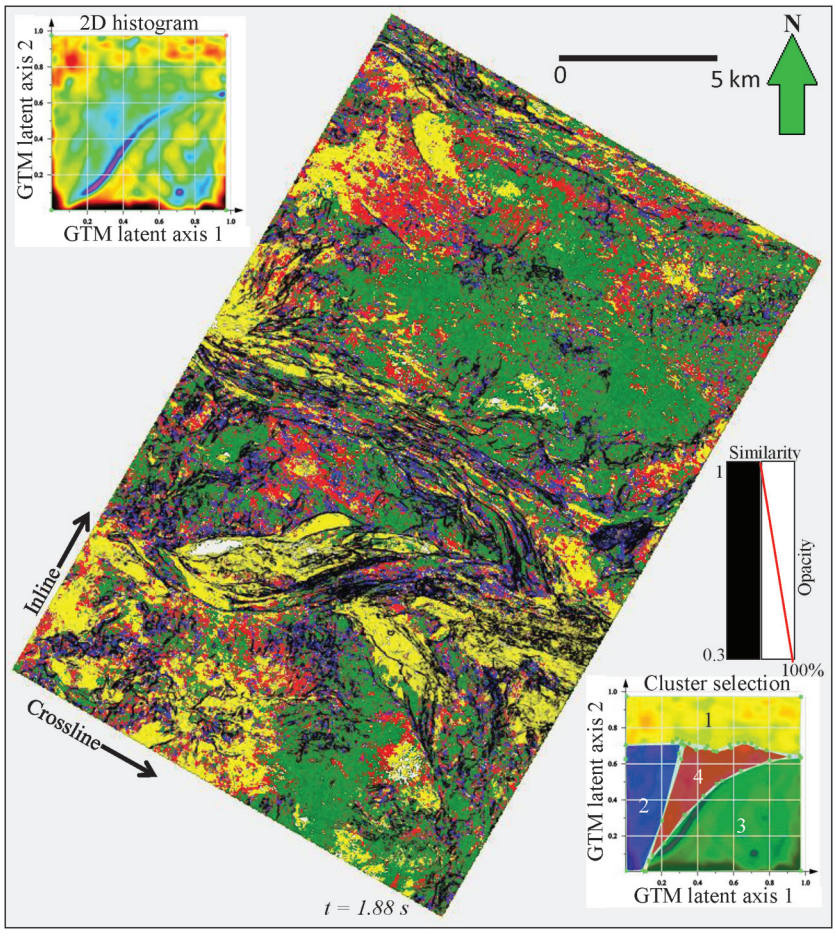

Figure 20. The same time slice through the GTM projections shown in the previous image but now displayed as four seismic facies. To do so, we first create two GTM "components" aligned with the original first two principal components. We then pick four colored polygons representing four seismic facies on the histogram generated using a commercial crossplot tool. This histogram is a map of the GTM posterior probability distribution in the latent space. The yellow polygon represents overbank deposits, the blue polygon represents channels/canyons, the green polygon represents slope fan deposits, and the red polygon represents everything else.

is somehow vague. This is the nature of unsupervised learning techniques, in that the clusters represent topological differences in the input data vectors, which are not necessarily the facies differences we wish to delineate. We can ameliorate this shortcoming by adding a posteriori supervision to the GTM manifold. The simplest way to add supervision is to compute the average attribute vectors about a given seismic facies and map it to the GTM crossplot. Then, the interpreter can manually define clusters on the 2D histogram by constructing one or more polygons (Figure 20), where we cluster the data into four facies: multistoried channels (blue), high-energy point bar and crevasse splay deposits (yellow), slope fans (green), and "everything else" (red). A more quantitative methodology is to mathematically project these average clusters onto the manifold and then cross-multiply the probability distribution of the control vectors against the probability distribution function of each data vector, thereby forming the Bhattacharyya distance (Roy et al., 2013, 2014). Such measures then provide a probability ranging between 0% and 100% as to whether the data vector at any seismic sample point is like the data vectors about well control (Roy et al., 2013, 2014) or like the average data vector within a facies picked by the interpreter.

The a posteriori supervision added to GTM is the critical prior supervision necessary for supervised classification, such as the ANN and SVM. In this study, we used the same four attributes as input for unsupervised and supervised learning techniques. Our supervision

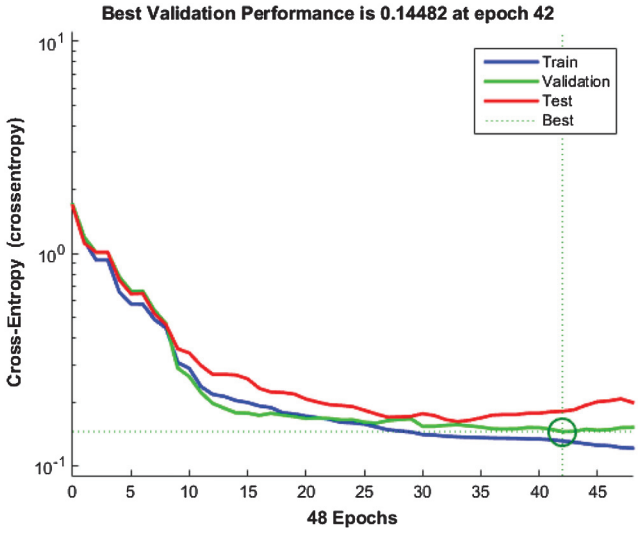

Figure 22. PNN errors through the training epochs. The neural network reaches its best performance at epoch 42.

Figure 21. Time slice at $t = 1.88$ s through the corendered peak spectral frequency, peak spectral magnitude, and Sobel filter similarity volumes. Seed points (training data) are shown with colors for the picked four facies: blue, multistoried channels; yellow, point bars and crevasse splays; red, channel flanks; and green, slope fans. Attribute vectors at these seed points are used as training data in supervised classification.

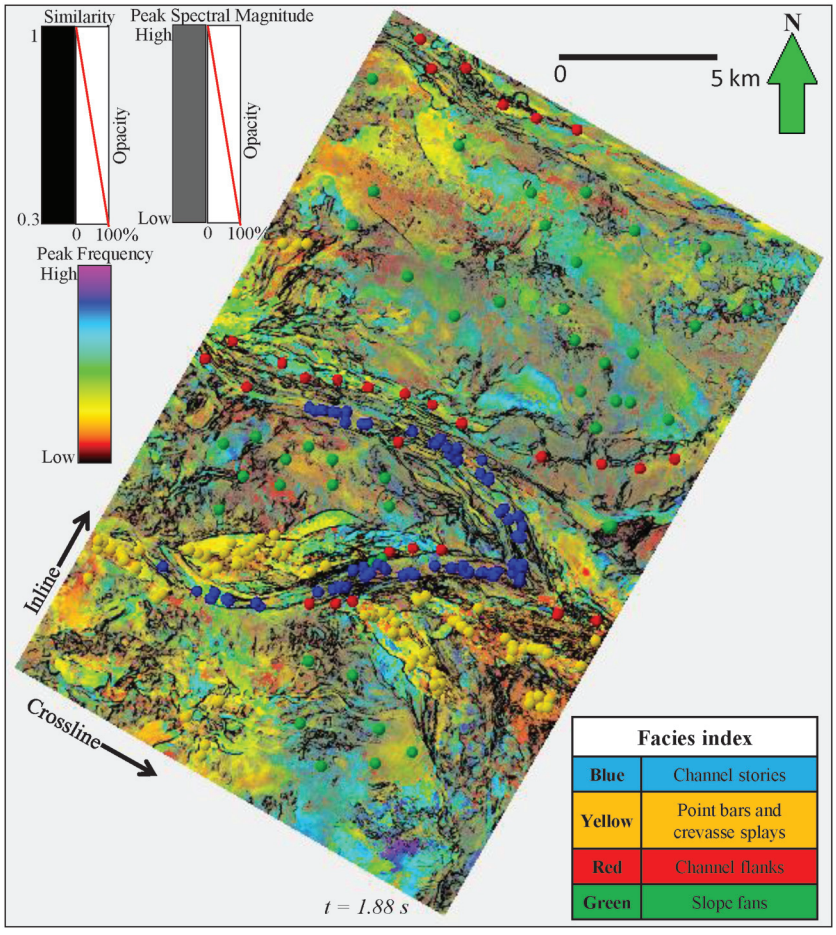

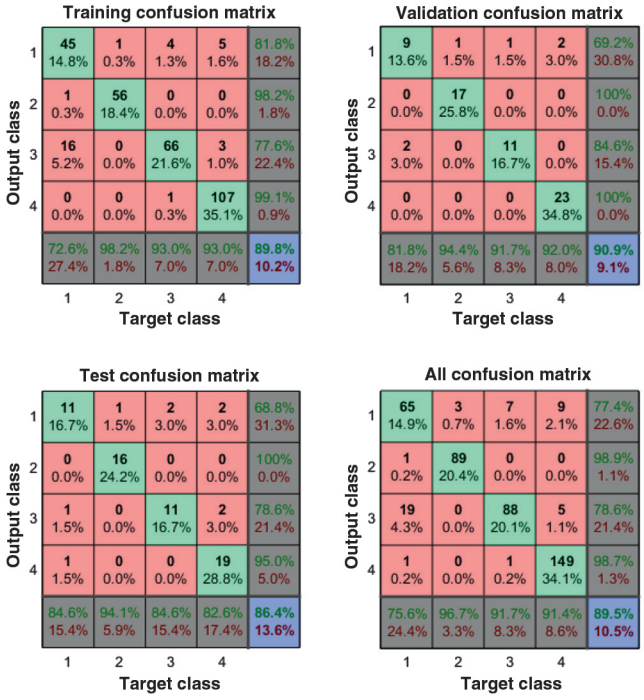

Figure 23. Confusion tables for the same PNN shown in Figure 21. From these tables, we find the training correctness to be 90%, the testing and cross-validation correctness to be 86%, and 91%, warranting a reliable prediction.

consists of picked seed points for the three main facies previously delineated using the unsupervised classification results, which are multistoried channel, point bar and crevasse splay deposits, and slope fans, plus an additional channel flank facies. The seed points are shown in Figure 21. Seed points should be picked with great caution to correctly represent the corresponding facies; any false picking (a seed point that does not belong to the intended facies) will greatly compromise the classification result. We then compute averages of the four input attributes within a 7 trace × 7 trace × 24 ms window about each seed point to generate a training table which consists of 4D input attribute vectors and 1D targets (the labeled facies).

For our ANN application, we used the neural networks toolbox in MATLAB, and generated a PNN composed of 20 neurons. Because of the relatively small size of the training data, the training process only took a second or so; however, because a PNN may converge to local minima, we are not confident that our first trained network has the best performance. Our workflow is then to rerun the training process 50 times and choose the network exhibiting the lowest training and cross-validation errors. Figures 22 and 23 show the PNN performance during training, whereas Figure 24 shows the PNN classification result. We notice that all the training,

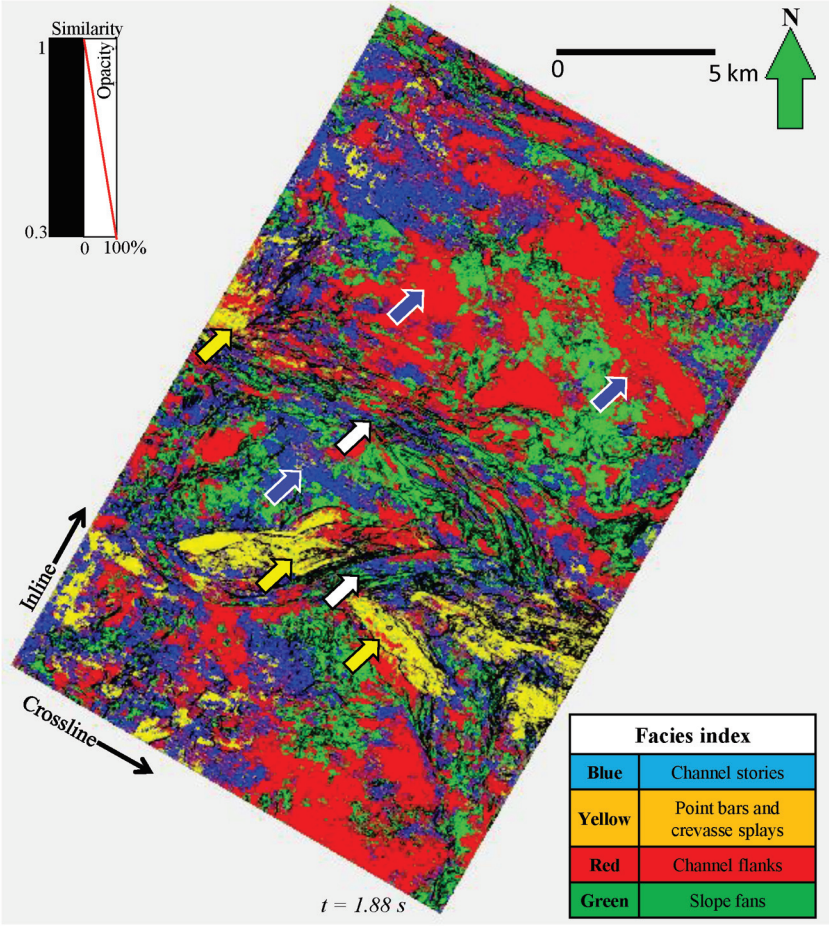

Figure 24. Time slice at $t = 1.88$ s through the ANN classification result. White arrows indicate channels/canyons. Yellow arrows indicate point bars and crevasse splays.

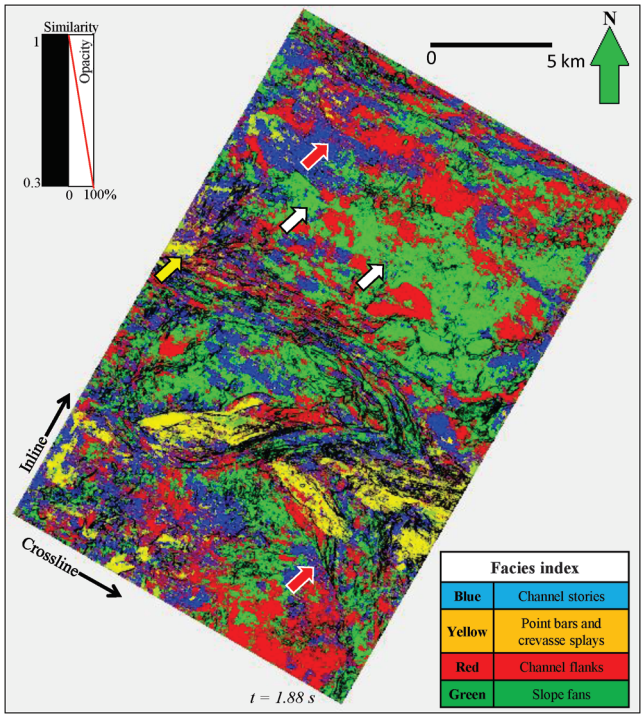

Figure 25. Time slice at $t = 1.88$ s through SVM classification result. White arrows indicate more correctly classified slope fans. The yellow arrow indicates crevasse splays. Red arrows show misclassifications due to the possible acquisition footprint.

testing, and cross-validation performance are acceptable, with the training and cross-validation correctness being approximately 90%, and the testing correctness being more than 86%. We identify blue channel stories within the relatively larger scale incised valleys (white arrows) and yellow point bars and crevasse splays (yellow arrows). However, many of the slope fan deposits are now classified as channel flanks or multistoried channels (blue arrows), which need to be further calibrated with well-log data. Nevertheless, as a supervised learning technique, ANN provides classification with explicit geologic meaning, which is its primary advantage over unsupervised learning techniques.

Finally, we cluster our 4D input data using SVM, using the same training data (interpreter picks) as for ANN. The workflow is similar to ANN, in that we ran 20 passes of training, varying the Gaussian kernel standard deviation σ, and misclassification tolerance ε, parameters for each pass. These parameter choices are easier than selecting the number of neurons for ANN because the SVM algorithm solves a convex optimization problem that converges to a global minima. The training and cross-validation performance is comparable with that of the ANN, with roughly 92% training correctness and 85% cross-validation correctness. Figure 25 shows the SVM classification result at time $t = 1.88$ s. The SVM map follows the same pattern as

Figure 26. Time slice at $t = 1.88$ s through the inline dip component of the reflector dip. Inline dip magnitude provides a photolike image of the paleocanyons.

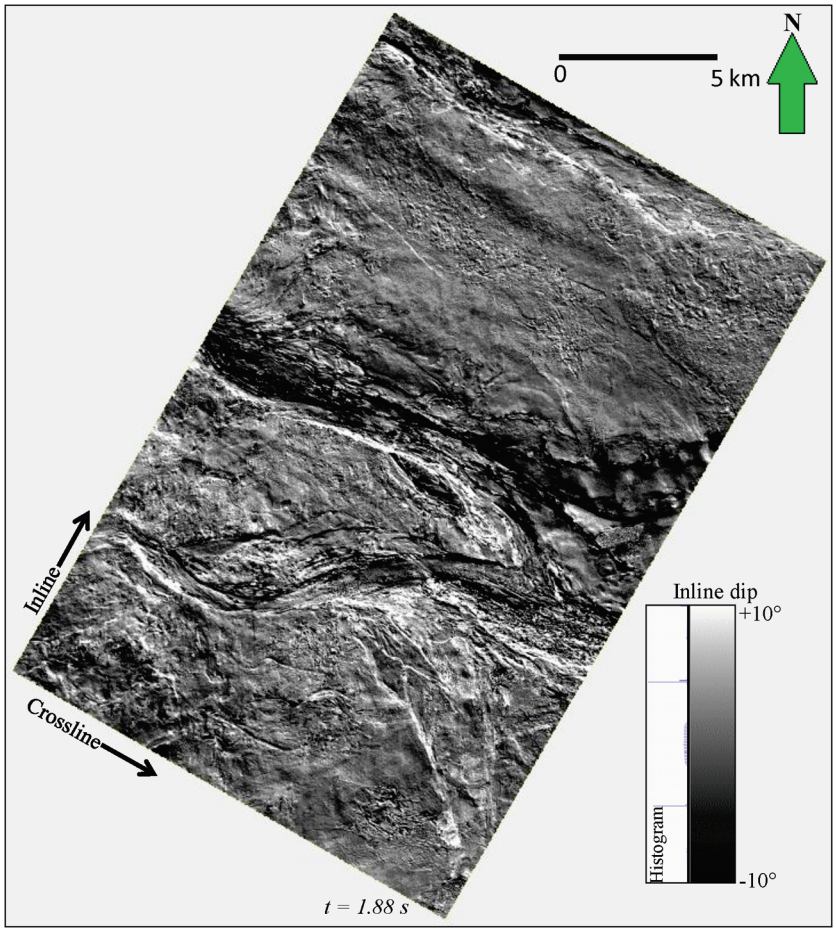

we have seen on the ANN map, but it is generally cleaner, with some differences in details. Compared with ANN, SVM successfully mapped more of the slope fans (white arrows), but it missed some crevasse splays that were correctly picked by ANN (yellow arrow). We also see a great amount of facies variation within the incised valleys, which is reasonable because of the multiple course changes of a paleochannel during its deposition that results in multiple channel stories. Finally, we note some red lines following northwestern–southeastern direction (red arrows), which correspond to the acquisition footprint.

Conclusions

In this paper, we have compared and contrasted some of the more important multiattribute facies classification tools, including four unsupervised (PCA, *k*-means, SOM, and GTM) and two supervised (ANN and SVM) learning techniques. In addition to highlighting the differences in assumptions and implementation, we have applied each method to the same Canterbury Basin survey, with the goal of delineating seismic facies in a turbidite system to demonstrate the effectiveness and weaknesses of each method. The *k*-means and SOM move the user-defined number of cluster centers toward the input data vectors. PCA is the simplest manifold method, where the data variability in our examples is approximated by a 2D plane defined by the first two eigenvectors. GTM is more accurately described as a mapping technique, like PCA, where the clusters are formed either in the human brain as part of visualization or through crossplotting and the construction of polygons. SOM and GTM manifolds deform to fit the *N*-dimensional data. In SOM, the cluster centers (prototype vectors) move along the manifold toward the data vectors, forming true clusters. In all four methods, any labeling of a given cluster to a given facies happens after the process is completed. In contrast, ANN and SVM build a specific relation between the input data vectors and a subset of user-labeled input training data vectors, thereby explicitly labeling the output clusters to the desired facies. Supervised learning is constructed from a limited group of training samples (usually at certain well locations or manually picked seed points), which generally are insufficient to represent all the lithologic and stratigraphic variations within a relatively large seismic data volume. A pitfall of supervised learning is that unforeseen clusters will be misclassified as clusters that have been chosen.

For this reason, unsupervised classification products can be used to construct not only an initial estimate of the number of classes, but also a validation tool to determine if separate clusters have been incorrectly lumped together. We advise computing unsupervised SOM or GTM prior to picking seed points for subsequent supervised learning, to clarify the topological differences mapped by our choice of attributes. Such mapping will greatly improve the picking confidence because the seed points are now confirmed by human experience and mathematical statistics.

The choice of the correct suite of attributes is critical. Specifically, images that are ideal for multiattribute visualization may be suboptimal for clustering. We made several poor choices in previous iterations of writing this paper. The image of the inline (southwest–northeast) structural dip illustrates this problem directly. Although a skilled interpreter sees a great deal of detail in Figure 26, there is no clear facies difference between positive and negative dips, such that this component of vector dip cannot be used to differentiate them. A better choice would be dip magnitude, except that a long-wavelength overprint (such as descending into the basin) would again bias our clustering in a manner that is unrelated to facies. Therefore, we tried to use relative changes in dip — curvedness and shape indices measure lateral changes in dip, and reflector convergence, which differentiates conformal from nonconformal reflectors.

Certain attributes should never be used in clustering. Phase, azimuth, and strike have circular distributions, in which a phase value of −180 indicates the same value as +180. No trend can be found. Although the shape index s is not circular, ranging between −1 and +1, the histogram has a peak about the ridge ($s = +0.5$) and about the valley ($s = -0.5$). We speculate that shape components may be more amenable to classification. Reflector convergence follows the same pattern as curvedness. For this reason, we only used curvedness as a representative of these three attributes. The addition of this choice improved our clustering.

Edge attributes such as Sobel filter similarity and coherence are not useful for the example shown here; instead, we have visually added them as an edge "cluster" and corendered with the images shown in Figures 15–21, 24, and 25. In contrast, when analyzing more chaotic features, such as salt domes and karst collapse, coherence is a good input to clustering algorithms. We do wish to provide an estimate of continuity and randomness to our clustering. To do so, use GLCM homogeneity as an input attribute.

Theoretically, no one technique is superior to all the others in every aspect, and each technique has its inherent advantages and defects. The *k*-means with a relatively small number of clusters is the easiest algorithm to implement, and it provides rapid interpretation, but it lacks the relation among clusters. SOM provides a generally more "interpreter-friendly" clustering result with topological connections among clusters, but it is computationally more demanding than *k*-means. GTM relies on probability theory and enables the interpreter to add a posteriori supervision by manipulating the data's posterior probability distribution; however, it is not widely accessible to the exploration geophysicist community. Rather than displaying the conventional cluster numbers (or labels), we suggest displaying the cluster coordinates projected onto the 2D SOM and GTM latent space axes. Doing so not only provides greater flexibil-

ity in constructing a 2D color bar, but it also provides data that can be further manipulated using 2D crossplot tools.

For the two supervised learning techniques, ANN suffers from the convergence problem and requires expertise to achieve the optimal performance, whereas the computation cost is relatively low. SVM is mathematically more robust and easier to train, but it is more computationally demanding.

Practically, if no software limitations are set, we can make suggestions on how an interpreter can incorporate these techniques to facilitate seismic facies interpretation at different exploration and development stages. To identify the main features in a recently acquired 3D seismic survey on which limited to no traditional structural interpretation is done, k-means is a good candidate for exploratory classification starting with a small K (typically $K = 4$) and gradually increase the number of class. As more data are acquired (e.g., well-log data and production data) and detailed structural interpretation has been performed, SOM or GTM focusing in the target formations will provide a more refined classification, which needs to be calibrated with wells. In the development stage, when most of the data have been acquired, with proper training processes, ANN and SVM provide targeted products, characterizing the reservoir by mimicking interpreters' behavior. Generally, SVM provides superior classification than ANN but at a considerably higher computational cost, so choosing between these two requires balancing performance and runtime cost. As a practical manner, no given interpretation software platform provides all five of these clustering techniques, such that many of the choices are based on software availability.

Because we wish this paper to serve as an inspiration of interpreters, we do want to reveal one drawback of our work: All the classifications are performed volumetrically but not along a certain formation. Such classification may be biased by the bonding formations above and below the target formation (if we do have a target formation), therefore contaminating the facies map. However, we want to make the point that such classification can happen at a very early stage of interpretation, when structural interpretation and well logs are very limited. And even in such a situation, we can still use classification techniques to generate facies volumes to assist subsequent interpretation.

In the 1970s and 1980s, much of the geophysical innovation in seismic processing and interpretation was facilitated by the rapid evolution of computer technology — from mainframes to minicomputers to workstations to distributed processing. We believe that similar advances in facies analysis will be facilitated by the rapid innovation in "big data" analysis, driven by the needs of marketing and security. Although we may not answer Turing's question, "Can machines think?" we will certainly be able to teach them how to emulate a skilled human interpreter.

Acknowledgments

We thank New Zealand Petroleum and Minerals for providing the Waka 3D seismic data to the public. Financial support for this effort and for the development of our own k-means, PCA, SOM, GTM, and SVM algorithms was provided by the industry sponsors of the Attribute-Assisted Seismic Processing and Interpretation Consortium at the University of Oklahoma. The ANN examples were run using MATLAB. We thank our colleagues F. Li, S. Verma, L. Infante, and B. Wallet for their valuable input and suggestions. All the 3D seismic displays were made using licenses to Petrel, provided to the University of Oklahoma for research and education courtesy of Schlumberger. Finally, we want to express our great respect to the people that have contributed the development of pattern recognition techniques in exploration geophysics field.

Appendix A

Mathematical details

In this appendix, we summarize many of the mathematical details defining the various algorithm implementations. Although insufficient to allow a straightforward implementation of each algorithm, we hope to more quantitatively illustrate the algorithmic assumptions, as well as algorithmic similarities and differences. Because k-means and ANNs have been widely studied, in this appendix, we only give some principal statistical background, and brief reviews of SOM, GTM, and PSVM algorithms involved in this tutorial. We begin this appendix by giving statistical formulations of the covariance matrix, principal components, and the Mahalanobis distance when applied to seismic attributes. We further illustrate the formulations and some necessary theory for SOM, GTM, ANN, and PSVM. Because of the extensive use of mathematical symbols and notations, a table of shared mathematical notations is given in Table A-1. All other symbols are defined in the text.

Covariance matrix, principal components, and the Mahalanobis distance

Given a suite of N attributes, the covariance matrix is defined as

$$C_{mn} = \frac{1}{J}\sum_{j=1}^{J}(a_{jm}(t_j, x_j, y_j) - \mu_m)(a_{jn}(t_j, x_j, y_j) - \mu_n), \tag{A-1}$$

where a_{jm} and a_{jn} are the mth and nth attributes, J is the total number of data vectors, and where

$$\mu_n = \frac{1}{J}\sum_{j=1}^{J} a_{jn}(t_j, x_j, y_j), \tag{A-2}$$

is the mean of the nth attribute. If we compute the eigenvalues λ_i and eigenvectors $\mathbf{v}_i$ of the real, symmetric

covariance matrix $\mathbf{C}$, the ith principal component at data vector j is defined as

$$p_{ji} = \sum_{n=1}^{N} a_{jn}(t_j, x_j, y_j) v_{ni}, \tag{A-3}$$

where v_{ni} indicates the nth attribute component of the ith eigenvector. In this paper, the first two eigenvectors and eigenvalues are also used to construct an initial model in the SOM and GTM algorithms.

The Mahalanobis distance r_{jq} of the jth sample from the qth cluster center, θ_q is defined as

$$r_{jq}^2 = \sum_{n=1}^{N}\sum_{m=1}^{N}(a_{jn} - \theta_{nq}) C_{nm}^{-1} (a_{jm} - \theta_{mq}), \tag{A-4}$$

where the inversion of the covariance matrix $\mathbf{C}$ takes place prior to extracting the mnth element.

Self-organizing maps

Rather than computing the Mahalanobis distance, the SOM and GTM first normalize the data using a Z-scale. If the data exhibit an approximately Gaussian distribution, the Z-scale of the nth attribute is obtained by subtracting the mean and dividing by the standard deviation (the square root of the diagonal of the covariance matrix $\mathbf{C}_{nn}$). To Z-scale non-Gaussian distributed data, such as coherence, one needs to first break down the data using histograms that approximate a Gaussian. The objective of the SOM algorithm is to map the input seismic attributes onto a geometric manifold called the *self-organized map*. The SOM manifold is defined by a suite of prototype vectors $\mathbf{m}_k$ lying on a lower dimensional (in our case, 2D) surface, which fit the N-dimensional attribute data. The prototype vectors $\mathbf{m}_k$ are typically arranged in 2D hexagonal or rectangular structure maps that preserve their original neighborhood relationship, such that neighboring prototype vectors represent similar data vectors. The number of prototype vectors in the 2D map determines the effectiveness and generalization of the algorithm. One strategy is to estimate the number of initial clusters, and then to either divide or join clusters based on distance criteria. In our case, we follow Gao (2007) and overdefine the number of clusters to be the maximum number of colors supported by our visualization software. Interpreters then either use their color perception or construct polygons on 2D histograms to define a smaller number of clusters.

Our implementation of the SOM algorithm is summarized in Figure A-1. After computing Z-scores of the input data, the initial manifold is defined to be a plane defined by the two first principal components. Prototype vectors $\mathbf{m}_k$ are defined on a rectangular grid to the first two eigenvalues to range between $\pm 2(\lambda_1)^{1/2}$ and $\pm 2(\lambda_2)^{1/2}$. The seismic attribute data are then compared with each of the prototype vectors, finding the nearest one. This prototype vector and its nearest neighbors (those that fall within a range σ, defining a Gaussian perturbation) are moved toward the data point. After all the training vectors have been examined, the neighborhood radius σ is reduced. Iterations continue until σ approaches the distance between the original prototype vectors. Given this background, Kohonen (2001) defines the SOM training algorithm using the following five steps:

1) Randomly choose a previously Z-scored input attribute vector $\mathbf{a}_j$ from the set of input vectors.
2) Compute the Euclidean distance between this vector $\mathbf{a}_j$ and all prototype vectors $\mathbf{m}_k$, $k = 1,2, \ldots, K$. The prototype vector that has the minimum distance to the input vector $\mathbf{a}_j$ is defined to be the "winner" or the best matching unit, $\mathbf{m}_b$:

$$\|\mathbf{a}_j - \mathbf{m}_b\| = \min_k \{\|\mathbf{a}_j - \mathbf{m}_k\|\}. \tag{A-5}$$

Table A-1. List of shared mathematical symbols.

Variable name	Definition
n and N	Attribute index and number of attributes
j and J	Voxel (attribute vector) index and number of voxels
k and K	Manifold index and number of grid points
$\mathbf{a}_j$	The jth attribute data vector
$\mathbf{p}$	Matrix of principal components
C	Attribute covariance matrix
μ_n	Mean of the nth attribute
λ_m and $\mathbf{v}_m$	The mth eigenvalue and eigenvector pair
$\mathbf{m}_k$	The kth grid point lying on the manifold (prototype vector for SOM, or Gaussian center for GTM)
$\mathbf{u}_k$	The kth grid point lying on the latent space
r_{jk}	The Mahalanobis distance between the jth data vector and the kth cluster center or manifold grid point
$\mathbf{I}$	Identity matrix of dimension defined in the text

3) Update the winner prototype vector and its neighbors. The updating rule for the weight of the kth prototype vector inside and outside the neighborhood radius $\sigma(t)$ is given by

$$\mathbf{m}_k(t+1) = \begin{cases} \mathbf{m}_k(t) + \alpha(t) h_{bk}(t)[\mathbf{a}_j - \mathbf{m}_k(t)], & \text{if } \|\mathbf{r}_k - \mathbf{r}_b\| \le \sigma(t), \\ \mathbf{m}_k(t), & \text{if } \|\mathbf{r}_k - \mathbf{r}_b\| > \sigma(t), \end{cases} \tag{A-6}$$

where the neighborhood radius defined as $\sigma(t)$ is predefined for a problem and decreases with each iteration t. Here, $\mathbf{r}_b$ and $\mathbf{r}_k$ are the position vectors of the winner prototype vector $\mathbf{m}_b$ and the kth prototype vector $\mathbf{m}_b$, respectively. We also define the neighborhood function $h_{bk}(t)$, the exponential learning function $\alpha(t)$, and the length of training T. The $h_{bk}(t)$ and $\alpha(t)$ decrease with each iteration in the learning process and are defined as

$$h_{bk}(t) = e^{-(\|\mathbf{r}_b - \mathbf{r}_k\|^2 / 2\sigma^2(t)}, \tag{A-7}$$

and

$$\alpha(t) = \alpha_0 \left(\frac{0.005}{\alpha_0} \right)^{t/T}. \tag{A-8}$$

4) Iterate through each learning step (steps [1–3]) until the convergence criterion (which depends on the predefined lowest neighborhood radius and the minimum distance between the prototype vectors in the latent space) is reached.
5) Project the prototype vectors onto the first two principal components and color code using a 2D color bar (Matos et al., 2009).

Generative topological mapping

In GTM, the grid points of our 2D deformed manifold in N-dimensional attribute space define the centers, $\mathbf{m}_k$, of Gaussian distributions of variance $\sigma^2 = \beta^{-1}$. These centers $\mathbf{m}_k$ are in turn projected onto a 2D latent space, defined by a grid of nodes $\mathbf{u}_k$ and nonlinear basis functions $\mathbf{\Phi}$:

$$\mathbf{m}_k = \sum_{m=1}^{M} \mathbf{W}_{km} \Phi_m(\mathbf{u}_k), \tag{A-9}$$

where $\mathbf{W}$ is a $K \times M$ matrix of unknown weights, $\Phi_m(\mathbf{u}_k)$ is a set of M nonlinear basis functions, $\mathbf{m}_k$ are vectors defining the deformed manifold in the N-dimensional data space, and $k = 1,2, \ldots, K$ is the number of grid points arranged on a lower L-dimensional latent space (in our case, $L = 2$). A noise model (the probability of the existence of a particular data vector $\mathbf{a}_j$ given weights $\mathbf{W}$ and inverse variance β) is introduced for each measured data vector. The probability density function p is represented by a suite of K radially symmetric N-dimensional Gaussian functions centered about $\mathbf{m}_k$ with variance of $1/\beta$:

$$p(\mathbf{a}_j | \mathbf{W}, \beta) = \sum_{k=1}^{K} \frac{1}{K} \left(\frac{\beta}{2\pi} \right)^{\frac{N}{2}} e^{-\frac{\beta}{2}\|\mathbf{m}_k - \mathbf{a}_j\|^2}. \tag{A-10}$$

The prior probabilities of each of these components are assumed to be equal with a value of $1/K$, for all data vectors $\mathbf{a}_j$. Figure 4 illustrates the GTM mapping from an $L = 2$D latent space to the 3D data space.

The probability density model (GTM model) is fit to the data $\mathbf{a}_j$ to find the parameters $\mathbf{W}$ and β using a maximum likelihood estimation. One popular technique used in parameter estimations is the EM algorithm. Using Bayes' theorem and the current values of the GTM

Figure A-1. The SOM workflow.

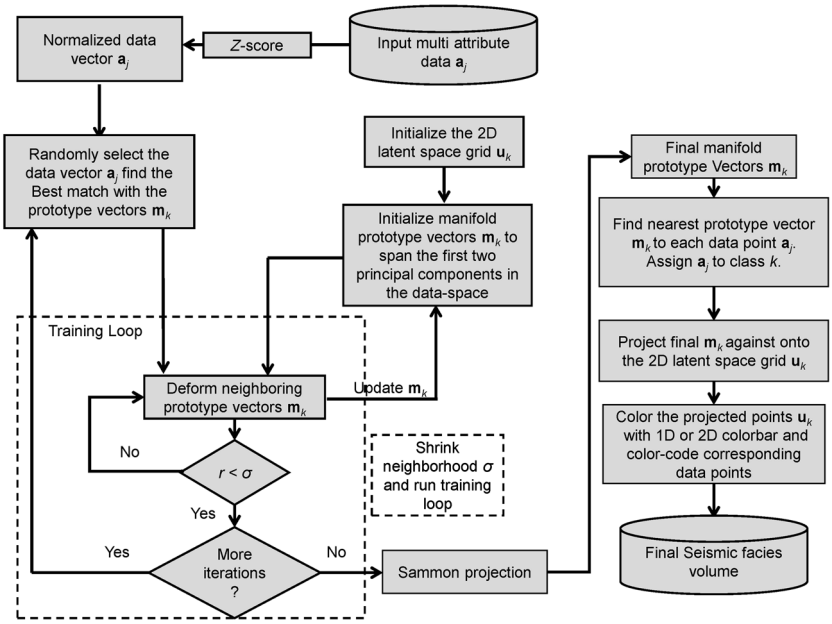

model parameters $\mathbf{W}$ and β, we calculate the $J \times K$ posterior probability or responsibility, R_{jk}, for each of the K components in latent space for each data-vector:

$$R_{jk} = \frac{e^{-\frac{\beta}{2}\|\mathbf{m}_k - \mathbf{a}_j\|^2}}{\sum_i e^{-\frac{\beta}{2}\|\mathbf{m}_i - \mathbf{a}_j\|^2}}. \tag{A-11}$$

Equation A-11 forms the "E-step" or expectation step in the EM algorithm. The E-step is followed by the maximization or "M-step," which uses these responsibilities to update the model for a new weight matrix $\mathbf{W}$ by solving a set of linear equations (Dempster et al., 1977):

$$\left(\mathbf{\Phi}^T\mathbf{G}\mathbf{\Phi} + \frac{\alpha}{\beta}\mathbf{I}\right)\mathbf{W}_{\text{new}}^T = \mathbf{\Phi}^T\mathbf{R}\mathbf{X}, \tag{A-12}$$

where $G_{kk} = \sum_{j=1}^{J} R_{jk}$ are the nonzero elements of the $K \times K$ diagonal matrix $\mathbf{G}$, $\mathbf{\Phi}$ is a $K \times M$ matrix with elements $\mathbf{\Phi} = \Phi_m(\mathbf{u}_k)$, α is a regularization constant to avoid division by zero, and $\mathbf{I}$ is the $M \times M$ identity matrix.

The updated value of β is given by

$$\frac{1}{\beta_{\text{new}}} = \frac{1}{JN}\sum_{j=1}^{J}\sum_{k=1}^{K} R_{jk}\|\mathbf{W}_{\text{km}_{\text{new}}}\Phi_m(\mathbf{u}_k) - \mathbf{a}_j\|^2. \tag{A-13}$$

The initialization of $\mathbf{W}$ is done so that the initial GTM model approximates the principal components (largest eigenvectors) of the input data, $\mathbf{a}_j$. The value of β^{-1} is initialized to be the larger of the $(L+1)$th eigenvalue from PCA, where L is the dimension of the latent space. In Figure 4, $L = 2$, such that we initialize β^{-1} to be the inverse of the third eigenvalue. Figure A-2 summarizes this workflow.

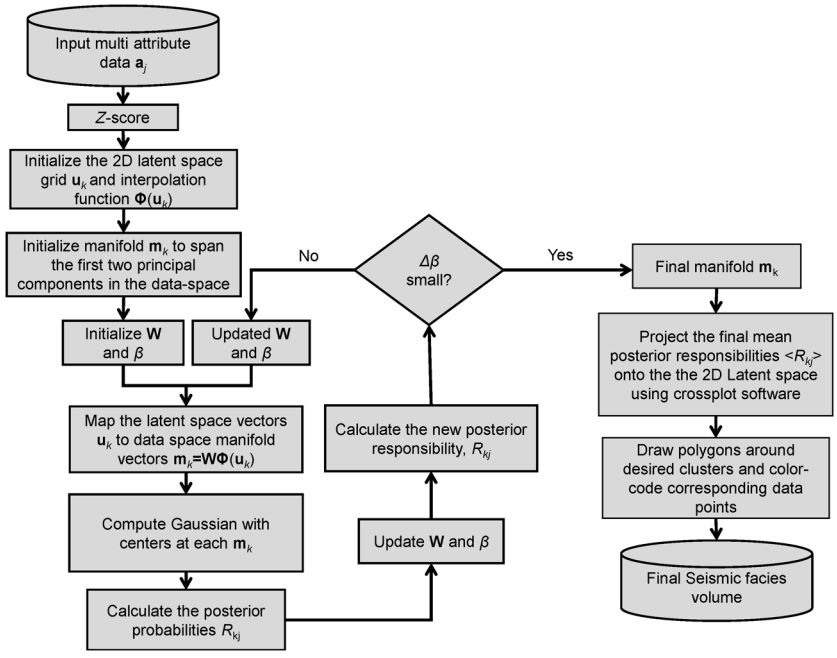

Figure A-2. The GTM workflow.

Artificial neural networks

ANNs are a class of pattern-recognition algorithm that were derived separately in different fields, such as statistics and artificial intelligence. ANNs are easily accessible for most of geophysical interpreters, so we only provide a general workflow of applying an ANN to seismic facies classification for completeness of this tutorial. The workflow is shown in Figure A-3.

Proximal support vector machines

Because SVMs are originally developed to solve binary classification problems, the arithmetic we begin with a summary of the arithmetic describing a binary PSVM classifier.

Similarly to SVM, a PSVM decision condition is defined as (Figure 7):

$$\mathbf{x}^T\boldsymbol{\omega} - \gamma \begin{cases} > 0, & \mathbf{x} \in X+, \\ = 0, & \mathbf{x} \in X+ \text{ or } X-, \\ < 0, & \mathbf{x} \in X-, \end{cases} \tag{A-14}$$

where $\mathbf{x}$ is an N-dimensional attribute vector to be classified, ω is a $N \times 1$ vector implicitly defines the normal of the decision-boundary in the higher-dimensional space, γ defines the location of the decision-boundary, and "$X+$" and "$X-$" indicate the two classes of the binary classification. PSVM solves an optimization problem and takes the form of (Fung and Mangasarian, 2001):

$$\min_{\boldsymbol{\omega},\gamma,\mathbf{y}} \varepsilon \frac{1}{2}\|\mathbf{y}\|^2 + \frac{1}{2}(\boldsymbol{\omega}^T\boldsymbol{\omega} + \gamma^2), \tag{A-15}$$

subject to

$$\mathbf{D}(\mathbf{a}\boldsymbol{\omega} - \mathbf{e}\gamma) + \mathbf{y} = \mathbf{e}. \tag{A-16}$$

In this optimization problem, $\mathbf{y}$ is a $J \times 1$ error variable and $\mathbf{a}$ is a $J \times N$ sample matrix composed of J attribute vectors, which can be divided into two classes, $X+$ and $X-$. The D is a $J \times J$ diagonal matrix of labels with a diagonal composed of $+1$ for $X+$ and -1 for $X-$. The ε is a nonnegative parameter. Finally, $\mathbf{e}$ is a $J \times 1$ column vector of ones. This optimization problem can be solved by a $J \times 1$ Lagrangian multiplier $\mathbf{t}$:

$$L(\boldsymbol{\omega}, \gamma, \mathbf{y}, \mathbf{t}) = \varepsilon \frac{1}{2}\|\mathbf{y}\|^2 + \frac{1}{2}(\boldsymbol{\omega}^T\boldsymbol{\omega} + \gamma^2) - \mathbf{t}^T(\mathbf{D}(\mathbf{a}\boldsymbol{\omega} - \mathbf{e}\gamma) + \mathbf{y} - \mathbf{e}). \tag{A-17}$$

By setting the gradients of L to zero, we obtain expressions for $\boldsymbol{\omega}$, γ and $\mathbf{y}$ explicitly in the knowns and $\mathbf{t}$, where $\mathbf{t}$ can further be represented by $\mathbf{a}$, D and ε. Then, by substituting ω in equations A-15 and A-16 using its dual equivalent $\boldsymbol{\omega} = \mathbf{a}^T\mathbf{D}\mathbf{t}$, we can arrive at (Fung and Mangasarian, 2001)

$$\min_{\omega,\gamma,\mathbf{y}} \varepsilon \frac{1}{2}\|\mathbf{y}\|^2 + \frac{1}{2}(\mathbf{t}^T\mathbf{t} + \gamma^2), \tag{A-18}$$

subject to

$$\mathbf{D}(\mathbf{a}\mathbf{a}^T\mathbf{D}\mathbf{t} - \mathbf{e}\gamma) + \mathbf{y} = \mathbf{e}. \tag{A-19}$$

Equations A-18 and A-19 provide a more desirable version of the optimization problem because one can now insert kernel methods to solve nonlinear classification problems made possible by the term $\mathbf{a}\mathbf{a}^T$ in equation A-19. Using the Lagrangian multiplier again (this time we denote the multiplier as $\boldsymbol{\tau}$), we can minimize the new optimization problem against $\mathbf{t}$, γ, $\mathbf{y}$, and $\boldsymbol{\tau}$. By setting the gradients of these four variables to zero, we can express $\mathbf{t}$, γ, and $\mathbf{y}$ explicitly by $\boldsymbol{\tau}$ and other knowns, where $\boldsymbol{\tau}$ is solely a dependent on the data matrices. Then, for N-dimensional attribute vector $\mathbf{x}$, we write the decision conditions as

$$\mathbf{x}^T\mathbf{a}^T\mathbf{D}\mathbf{t} - \gamma \begin{cases} > 0, & \mathbf{x} \in X+, \\ = 0, & \mathbf{x} \in X+ \text{ or } X-, \\ < 0, & \mathbf{x} \in X-, \end{cases} \tag{A-20}$$

with

$$\mathbf{t} = \mathbf{D}\mathbf{K}^T\mathbf{D}\left(\frac{\mathbf{I}}{\varepsilon} + \mathbf{G}\mathbf{G}^T\right)^{-1}\mathbf{e}, \tag{A-21}$$

$$\gamma = \mathbf{e}^T\mathbf{D}\left(\frac{\mathbf{I}}{\varepsilon} + \mathbf{G}\mathbf{G}^T\right)^{-1}\mathbf{e}, \tag{A-22}$$

and

$$\mathbf{G} = \mathbf{D}[\mathbf{K} \quad -\mathbf{e}]. \tag{A-23}$$

Instead of $\mathbf{a}$, we have $\mathbf{K}$ in equations A-21 and A-23, which is a Gaussian kernel function of $\mathbf{a}$ and $\mathbf{a}^T$ that has the form of

$$\mathbf{K}(\mathbf{a}, \mathbf{a}^T)_{ij} = \exp(-\sigma\|\mathbf{a}_{i\bullet}^T - \mathbf{a}_{j\bullet}^T\|^2), \quad i,j \in [1,J], \tag{A-24}$$

where σ is a scalar parameter. Finally, by replacing $\mathbf{x}^T\mathbf{a}^T$ by its corresponding kernel expression, the decision condition can be written as

$$\mathbf{K}(\mathbf{x}^T, \mathbf{a}^T)\mathbf{D}\mathbf{t} - \gamma \begin{cases} > 0, & \mathbf{x} \in X+, \\ = 0, & \mathbf{x} \in X+ \text{ or } X-, \\ < 0, & \mathbf{x} \in X-, \end{cases} \tag{A-25}$$

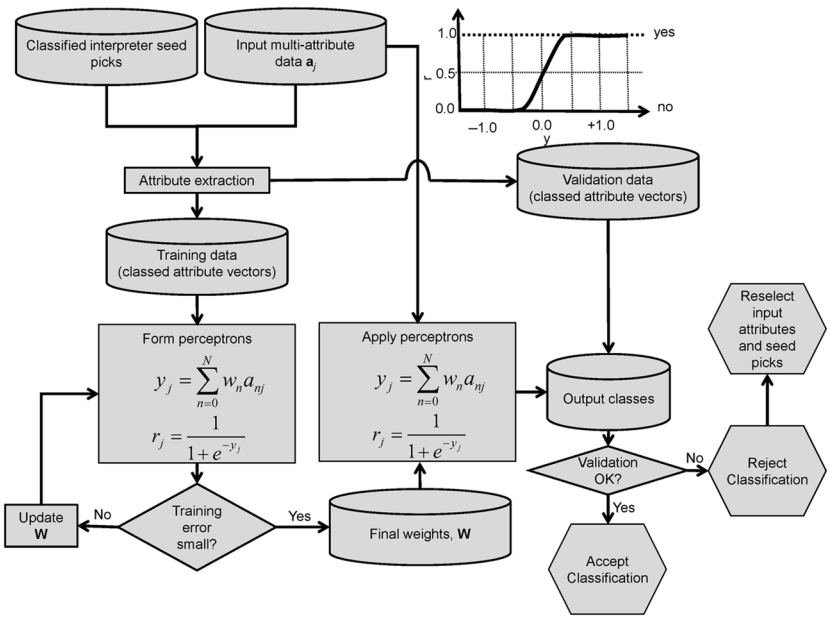

Figure A-3. The ANN workflow.

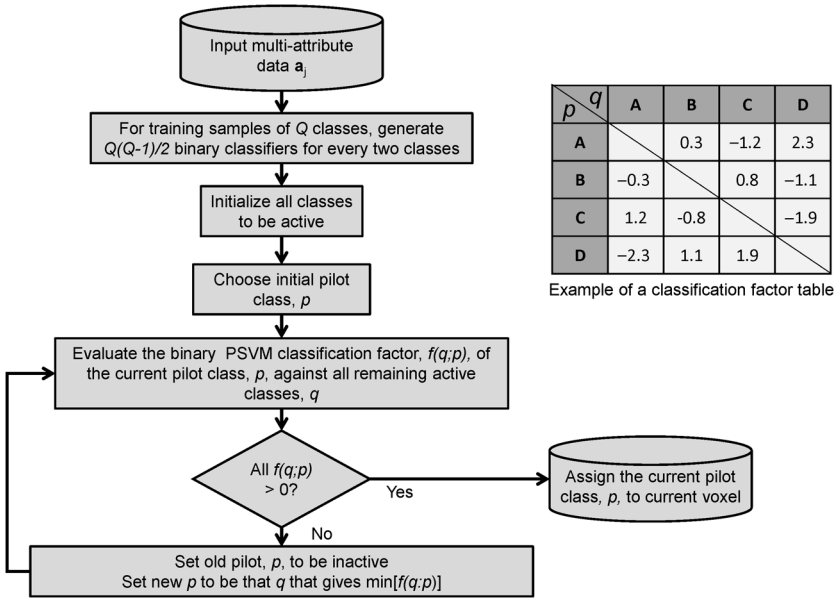

p \ q	A	B	C	D
A		0.3	−1.2	2.3
B	−0.3		0.8	−1.1
C	1.2	-0.8		−1.9
D	−2.3	1.1	1.9	

Example of a classification factor table

Figure A-4. The PSVM workflow.

and

$$\mathbf{K}(\mathbf{x}^T, \mathbf{a}^T)_{ij} = \exp(-\sigma\|\mathbf{x} - \mathbf{a}_{i\bullet}^T\|^2), \quad i \in [1, J]. \quad \text{(A-26)}$$

The formulations above represent a nonlinear PSVM classifier.

To extend this binary classifier to handle multiclass classification problems, some strategies have been developed by researchers, which generally fall into three categories: "one-versus-all," "one-versus-one," and "all together." For Q classes, the former two strategies build a suite of binary classifiers individually: $(Q(Q-1)/2$ for the one-versus-one and Q for the one-versus-all algorithm, and we then use these classifiers to construct the final classification decision. The all-together attempts to solve multiclass problem in one step. Hsu and Lin (2002) find one-versus-one method to be superior for large problems. There are two particular algorithms for one-versus-one strategies, namely, the "max wins" (Kreßel, 1999) and directed acyclic graph (Platt et al., 2000) algorithms. Both algorithms provide comparable results while surpassing the one-versus-all method in accuracy and computational efficiency.

Our approach uses a classification factor table to assign classes to unknown samples (Figure A-4). A classification factor of an unknown sample point for a certain pilot class "X" is the normalized distance to the binary decision boundary between X and the other class used when generating this binary decision boundary. An example of a classification factor table is shown in Figure A-4, and based on this table, the unknown sample point belongs to class "D."

References

Al-Anazi, A., and I. D. Gates, 2010, A support vector machine algorithm to classify lithofacies and model permeability in heterogeneous reservoirs: Engineering Geology, **114**, 267–277, doi: 10.1016/j.enggeo.2010.05.005.

Balch, A. H., 1971, Color sonagrams: A new dimension in seismic data interpretation: Geophysics, **36**, 1074–1098, doi: 10.1190/1.1440233.

Barnes, A. E., and K. J. Laughlin, 2002, Investigation of methods for unsupervised classification of seismic data: 72nd Annual International Meeting, SEG, Expanded Abstracts, 2221–2224.

Bennett, K. P., and A. Demiriz, 1999, Semi-supervised support vector machines: *in* M. S. Kearns, S. A. Solla, and D. A. Cohn, eds., Advances in Neural Information Processing Systems 11: Proceedings of the 1998 Conference, MIT Press, 368–374.

Bishop, C. M., 2006, Pattern recognition and machine learning: Springer.

Bishop, C. M., M. Svensen, and C. K. I. Williams, 1998, The generative topographic mapping: Neural Computation, **10**, 215–234, doi: 10.1162/089976698300017953.

Chopra, S., and K. J. Marfurt, 2007, Seismic attributes for prospect identification and reservoir characterization: SEG.

Coleou, T., M. Poupon, and K. Azbel, 2003, Unsupervised seismic facies classification: A review and comparison of techniques and implementation: The Leading Edge, **22**, 942–953, doi: 10.1190/1.1623635.

Corradi, A., P. Ruffo, A. Corrao, and C. Visentin, 2009, 3D hydrocarbon migration by percolation technique in an alternative sand-shale environment described by a seismic facies classification volume: Marine and Petroleum Geology, **26**, 495–503, doi: 10.1016/j.marpetgeo.2009.01.002.

Cortes, C., and V. Vapnik, 1995, Support-vector networks: Machine Learning, **20**, 273–297, doi: 10.1023/A:1022627411411.

Cristianini, N., and J. Shawe-Taylor, 2000, An introduction to support vector machines and other kernel-based learning methods: Cambridge University Press.

Dempster, A. P., N. M. Laird, and D. B. Rubin, 1977, Maximum likelihood from incomplete data via the EM algorithm: Journal of the Royal Statistical Society, Series B, **39**, 1–38.

Duda, R. O., P. E. Hart, and D. G. Stork, 2001, Pattern classification, 2nd ed.: John Wiley & Sons.

Eagleman, D., 2012, Incognito: The secret lives of the brain: Pantheon Books.

Forgy, E. W., 1965, Cluster analysis of multivariate data: Efficiency vs interpretability of classifications: Biometrics, **21**, 768–769.

Fung, G., and O. L. Mangasarian, 2001, Proximal support vector machine classifiers: Proceedings of the Seventh ACM SIGKDD International Conference on Knowledge Discovery and Data Mining, ACM 2001, 77–86.

Fung, G. M., and O. L. Mangasarian, 2005, Multicategory proximal support vector machine classifiers: Machine Learning, **59**, 77–97, doi: 10.1007/s10994-005-0463-6.

Gao, D., 2007, Application of three-dimensional seismic texture analysis with special reference to deep-marine facies discrimination and interpretation: An example from offshore Angola, West Africa: AAPG Bulletin, **91**, 1665–1683, doi: 10.1306/08020706101.

Honório, B. C. Z., A. C. Sanchetta, E. P. Leite, and A. C. Vidal, 2014, Independent component spectral analysis: Interpretation, **2**, no. 1, SA21–SA29, doi: 10.1190/INT-2013-0074.1.

Hsu, C., and C. Lin, 2002, A comparison of methods for multiclass support vector machines: IEEE Transactions on Neural Networks, **13**, 732–744, doi: 10.1109/TNN.2002.1000139.

Huang, Z., J. Shimeld, M. Williamson, and J. Katsube, 1996, Permeability prediction with artificial neural network modeling in the Ventura gas field, offshore eastern Canada: Geophysics, **61**, 422–436, doi: 10.1190/1.1443970.

Jancey, R. C., 1966, Multidimensional group analysis: Australian Journal of Botany, **14**, 127–130, doi: 10.1071/BT9660127.

Justice, J. H., D. J. Hawkins, and D. J. Wong, 1985, Multidimensional attribute analysis and pattern recognition for seismic interpretation: Pattern Recognition, **18**, 391–399, doi: 10.1016/0031-3203(85)90010-X.

Kalkomey, C. T., T. Zhao, X. Jin, and K. J. Marfurt, 1997, Potential risks when using seismic attributes as predictors of reservoir properties: The Leading Edge, **16**, 247–251, doi: 10.1190/1.1437610.

Kohonen, T., 1982, Self-organized formation of topologically correct feature maps: Biological Cybernetics, **43**, 59–69, doi: 10.1007/BF00337288.

Kohonen, T., 2001, Self-organizing maps (3rd ed.): Springer-Verlag.

Kreßel, U., 1999, Pairwise classification and support vector machines: Advances in kernel methods — Support vector learning, *in* B. Schölkopf, C. J. C. Burges, and A. J. Smola, eds., Advances in kernel methods: MIT Press, 255–268.

Kuzma, H. A., and J. W. Rector, 2004, Nonlinear AVO inversion using support vector machines: 74th Annual International Meeting, SEG, Expanded Abstracts, 203–206.

Kuzma, H. A., and J. W. Rector, 2005, The Zoeppritz equations, information theory, and support vector machines: 75th Annual International Meeting, SEG, Expanded Abstracts, 1701–1704.

Kuzma, H. A., and J. W. Rector, 2007, Support vector machines implemented on a graphics processing unit: 77th Annual International Meeting, SEG, Expanded Abstracts, 2089–2092.

Li, J., and J. Castagna, 2004, Support vector machine (SVM) pattern recognition to AVO classification: Geophysical Research Letters, **31**, L02609, doi: 10.1029/2003GL019044.

Lim, J., 2005, Reservoir properties determination using fuzzy logic and neural networks from well data in offshore Korea: Journal of Petroleum Science and Engineering, **49**, 182–192, doi: 10.1016/j.petrol.2005.05.005.

Lubo, D., K. Marfurt, and V. Jayaram, 2014, Statistical characterization and geological correlation of wells using automatic learning Gaussian mixture models: Unconventional Resources Technology Conference, Extended Abstracts, 774–783.

MacQueen, J., 1967, Some methods for classification and analysis of multivariate observations: *in* L. M. Le Cam, and J. Neyman, eds.,Proceedings of the Fifth Berkeley Symposium on Mathematical Statistics and Probability, University of California Press, 281–297.

Mangasarian, O. L., and E. W. Wild, 2006, Multisurface proximal support vector machine classification via generalized eigenvalues: IEEE Transactions on Pattern Analysis and Machine Intelligence, **28**, 69–74, doi: 10.1109/TPAMI.2006.17.

Matos, M. C., K. J. Marfurt, and P. R. S. Johann, 2009, Seismic color self-organizing maps: Presented at 11th International Congress of the Brazilian Geophysical Society, Extended Abstracts.

Meldahl, P., R. Heggland, B. Bril, and P. de Groot, 1999, The chimney cube, an example of semi-automated detection of seismic objects by directive attributes and neural networks. Part I: Methodology: 69th Annual International Meeting, SEG, Expanded Abstracts, 931–934.

Mitchell, J., and H. L. Neil, 2012, OS20/20 Canterbury — Great South Basin TAN1209 voyage report: National Institute of Water and Atmospheric Research Ltd (NIWA).

Murat, M. E., and A. J. Rudman, 1992, Automated first arrival picking: A neural network approach: Geophysical Prospecting, **40**, 587–604, doi: 10.1111/j.1365-2478.1992.tb00543.x.

Nazari, S., H. A. Kuzma, and J. W. Rector, 2011, Predicting permeability from well log data and core measurements using support vector machines: 81st Annual International Meeting, SEG, Expanded Abstracts, 2004–2007.

Platt, J. C., N. Cristianini, and J. Shawe-Taylor, 2000, Large margin DAGs for multiclass classification: Advances in Neural Information Processing Systems, **12**, 547–553.

Röth, G., and A. Tarantola, 1994, Neural networks and inversion of seismic data: Journal of Geophysical Research, **99**, 6753–6768, doi: 10.1029/93JB01563.

Roy, A., 2013, Latent space classification of seismic facies: Ph.D. dissertation, The University of Oklahoma.

Roy, A., S. R. Araceli, J. T. Kwiatkowski, and K. J. Marfurt, 2014, Generative topographic mapping for seismic facies estimation of a carbonate wash, Veracruz Basin, Southern Mexico: Interpretation, **2**, no. 1, SA31–SA47, doi: 10.1190/INT-2013-0077.1.

Roy, A., B. L. Dowdell, and K. J. Marfurt, 2013, Characterizing a Mississippian tripolitic chert reservoir using 3D unsupervised and supervised multiattribute seismic facies analysis: An example from Osage County, Oklahoma: Interpretation, **1**, no. 2, SB109–SB124, doi: 10.1190/INT-2013-0023.1.

Russell, B., D. Hampson, J. Schuelke, and J. Quirein, 1997, Multiattribute seismic analysis: The Leading Edge, **16**, 1439–1443, doi: 10.1190/1.1437486.

Sammon, W. J., 1969, A nonlinear mapping for data structure analysis, IEEE Transactions on Computers, **C-18**, 401–409.

Schölkopf, B., and A. J. Smola, 2002, Learning with kernels: Support vector machines, regularization, optimization, and beyond: MIT Press.

Shawe-Taylor, J., and N. Cristianini, 2004, Kernel methods for pattern analysis: Cambridge University Press.

Sonneland, L., 1983, Computer aided interpretation of seismic data: 53rd Annual International Meeting, SEG, Expanded Abstracts, 546–549.

Strecker, U., and R. Uden, 2002, Data mining of 3D poststack attribute volumes using Kohonen self-organizing maps: The Leading Edge, **21**, 1032–1037, doi: 10.1190/1.1518442.

Taner, M. T., F. Koehler, and R. E. Sheriff, 1979, Complex seismic trace analysis: Geophysics, **44**, 1041–1063, doi: 10.1190/1.1440994.

Tong, S., and D. Koller, 2001, Support vector machine active learning with applications to text classification: Journal of Machine Learning Research, **2**, 45–66.

Torres, A., and J. Reveron, 2013, Lithofacies discrimination using support vector machines, rock physics and simultaneous seismic inversion in clastic reservoirs in the Orinoco Oil Belt, Venezuela: 83rd Annual International Meeting, SEG, Expanded Abstracts, 2578–2582.

Turing, A. M., 1950, Computing machinery and intelligence: Mind, **59**, 433–460, doi: 10.1093/mind/LIX.236.433.

Uruski, C. I., 2010, New Zealand's deepwater frontier: Marine and Petroleum Geology, **27**, 2005–2026, doi: 10.1016/j.marpetgeo.2010.05.010.

van der Baan, M., and C. Jutten, 2000, Neural networks in geophysical applications: Geophysics, **65**, 1032–1047, doi: 10.1190/1.1444797.

Verma, S., A. Roy, R. Perez, and K. J. Marfurt, 2012, Mapping high frackability and high TOC zones in the Barnett Shale: Supervised probabilistic neural network vs. unsupervised multi-attribute Kohonen SOM: 82nd Annual International Meeting, SEG, Expanded Abstracts, doi: 10.1190/segam2012-1494.1.

Wallet, C. B., M. C. Matos, and J. T. Kwiatkowski, 2009, Latent space modeling of seismic data: An overview: The Leading Edge, **28**, 1454–1459, doi: 10.1190/1.3272700.

Wang, G., T. R. Carr, Y. Ju, and C. Li, 2014, Identifying organic-rich Marcellus Shale lithofacies by support vector machine classifier in the Appalachian basin: Computers & Geosciences, **64**, 52–60, doi: 10.1016/j.cageo.2013.12.002.

West, P. B., R. S. May, E. J. Eastwood, and C. Rossen, 2002, Interactive seismic facies classification using textural attributes and neural networks: The Leading Edge, **21**, 1042–1049, doi: 10.1190/1.1518444.

Wong, K. W., Y. S. Ong, T. D. Gedeon, and C. C. Fung, 2005, Reservoir characterization using support vector machines: Presented at Computational Intelligence for Modelling, Control and Automation, International Conference on Intelligent Agents, Web Technologies and Internet Commerce, 354–359.

Yu, S., K. Zhu, and F. Diao, 2008, A dynamic all parameters adaptive BP neural networks model and its application on oil reservoir prediction: Applied Mathematics and Computation, **195**, 66–75, doi: 10.1016/j.amc.2007.04.088.

Zhang, B., T. Zhao, X. Jin, and K. J. Marfurt, 2015, Brittleness evaluation of resource plays by integrating petrophysical and seismic data analysis: Interpretation, **3**, no. 2, T81–T92, doi: 10.1190/INT-2014-0144.1.

Zhao, B., H. Zhou, and F. Hilterman, 2005, Fizz and gas separation with SVM classification: 75th Annual International Meeting, SEG, Expanded Abstracts, 297–300.

Zhao, T., V. Jayaram, K. J. Marfurt, and H. Zhou, 2014, Lithofacies classification in Barnett Shale using proximal support vector machines: 84th Annual International Meeting, SEG, Expanded Abstracts, 1491–1495.

Zhao, T., and K. Ramachandran, 2013, Performance evaluation of complex neural networks in reservoir characterization: Applied to Boonsville 3-D seismic data: 83rd

Annual International Meeting, SEG, Expanded Abstracts, 2621–2624.

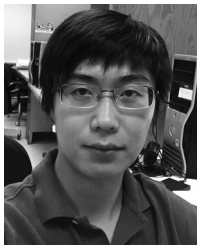

Tao Zhao received a B.S. (2011) in exploration geophysics from China University of Petroleum and an M.S. (2013) in geophysics from the University of Tulsa. He is currently pursuing Ph.D. in geophysics in the University of Oklahoma as a member of attribute assisted seismic processing and interpretation consortium. His current research interests include developing and applying pattern recognition and machine learning techniques on seismic data, unconventional shale resource play characterization, and seismic attributes development.

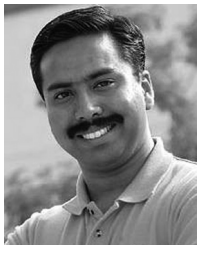

Vikram Jayaram received an M.S. (2004) and a Ph.D. (2009) in electrical engineering from the University of Texas at El Paso. Prior to joining the University of Oklahoma (OU), he was a postdoctoral fellow in computational radio-nuclide imaging at the University of Texas M.D. Anderson working on image reconstruction techniques for nuclear imaging. He was awarded the prestigious NASA Earth System Science doctoral fellowship, NGA, and Texas Instruments foundation scholarships to support his graduate studies. More recently, he has worked as a senior research geophysicist with Global Geophysical Services, Co-PI of academic industry consortium at OU, Oklahoma Geological Survey. While a graduate student, he also interned with Kodak Research Labs. He has authored more than 25 research papers and is currently serving as an assistant editor for the SEG/AAPG journal Interpretation. He is a member of IEEE Signal Processing Society, AGU, SEG, EAGE, AAPG, and a technical reviewer for several international conferences and journals in signal processing, machine learning and geophysics. His research interests include computer learning models for mathematical and physical exploitation in imaging, signal/image enhancement and interpretation, and big data analytics.

Atish Roy received a B.S. (2005) in physics from the University of Calcutta and an M.S. (2007) in applied geophysics from the Indian Institute of Technology, Bombay. After working for two years at Paradigm Geophysical, India, as a processing geophysicist, he joined the University of Oklahoma in 2009 to pursue a Ph.D. degree. There, he did research in the attribute-assisted seismic processing and interpretation research consortium led by Kurt J. Marfurt. In his research, he developed algorithms and workflows for unsupervised, supervised, and probabilistic seismic facies classification using multiattribute data. He received a Ph.D. in geophysics in the fall of 2013. Currently, he is working at BP as a geophysical analyst in the technology group. His research interests include pattern recognition, machine learning, seismic facies analysis, seismic attribute analysis, reservoir characterization, and subsurface imaging.

Kurt. J. Marfurt received a Ph.D. (1978) in applied geophysics from Columbia University's Henry Krumb School of Mines in New York, where he also served as an assistant professor for four years. He joined the University of Oklahoma (OU) in 2007 where he serves as the Frank and Henrietta Schultz Professor of Geophysics within the ConocoPhillips School of Geology and Geophysics. His primary research interest is in the development and calibration of new seismic attributes to aid in seismic processing, seismic interpretation, and reservoir characterization. His recent works focused on applying coherence, spectral decomposition, structure-oriented filtering, and volumetric curvature to mapping fractures and karst with a particular focus on resource plays. He worked 18 years in a wide range of research projects at Amoco's Tulsa Research Center, after which he joined the University of Houston for eight years as a professor of geophysics and the director of the Allied Geophysics Lab. He has received SEG best paper (for coherence), SEG best presentation (for seismic modeling) and as a coauthor with Satinder Chopra best SEG poster (for curvature), and best AAPG technical presentation. He also served as the EAGE/SEG Distinguished Short Course Instructor in 2006 (on seismic attributes). In addition to teaching and research duties at OU, he leads short courses on attributes for SEG and AAPG.